The Astrophysical Journal, 837:75 (25pp), 2017 March 1 https://doi.org/10.3847/1538-4357/aa60bc

Turbulent Transport in a Three-dimensional Solar Wind

D. Shiota[1], G. P. Zank[2], L. Adhikari[2], P. Hunana[2], D. Telloni[3], and R. Bruno[4]
[1] Institute for Space-Earth Environmental Research, Nagoya University, Nagoya, Aichi 464-8601, Japan; shiota@isee.nagoya-u.ac.jp
[2] Center for Space Plasma and Aeronomic Research (CSPAR), Department of Space Science, University of Alabama in Huntsville, Huntsville, AL 35805, USA
[3] INAF—Astrophysical Observatory of Torino, Via Osservatorio 20, I-10025 Pino Torinese, Italy
[4] INAF-IAPS Istituto di Astrofisica e Planetologia Spaziali, Via del Fosso del Cavaliere 100, I-00133 Roma, Italy
Received 2016 March 16; revised 2017 January 13; accepted 2017 February 13; published 2017 March 6

Abstract

Turbulence in the solar wind can play essential roles in the heating of coronal and solar wind plasma and the acceleration of the solar wind and energetic particles. Turbulence sources are not well understood and thought to be partly enhanced by interaction with the large-scale inhomogeneity of the solar wind and the interplanetary magnetic field and/or transported from the solar corona. To investigate the interaction with background inhomogeneity and the turbulence sources, we have developed a new 3D MHD model that includes the transport and dissipation of turbulence using the theoretical model of Zank et al. We solve for the temporal and spatial evolution of three moments or variables, the energy in the forward and backward fluctuating modes and the residual energy and their three corresponding correlation lengths. The transport model is coupled to our 3D model of the inhomogeneous solar wind. We present results of the coupled solar wind-turbulence model assuming a simple tilted dipole magnetic configuration that mimics solar minimum conditions, together with several comparative intermediate cases. By considering eight possible solar wind and turbulence source configurations, we show that the large-scale solar wind and IMF inhomogeneity and the strength of the turbulence sources significantly affect the distribution of turbulence in the heliosphere within 6 au. We compare the predicted turbulence distribution results from a complete solar minimum model with in situ measurements made by the *Helios* and *Ulysses* spacecraft, finding that the synthetic profiles of the turbulence intensities show reasonable agreement with observations.

Key words: magnetohydrodynamics (MHD) – solar wind – turbulence

1. Introduction

Turbulence in the solar wind over a wide range of spectral scales has been observed by many in situ measurements as fluctuations in the interplanetary magnetic field (IMF) and solar wind velocity since the pioneering studies of Coleman (1968) and Belcher & Davis (1971). In situ measurements show that the solar wind exhibits a global-scale inhomogeneity in magnetohydrodynamic (MHD) parameters, which may reflect differences in energy deposition (heating and acceleration) as the solar wind escapes from the solar corona (Tu 1987; Tu & Marsch 1990, 1997; Zhou & Matthaeus 1990). The turbulence in the solar corona and solar wind is the most plausible candidate to play a significant role in the deposition of energy throughout the large-scale heliosphere.

A typical spectrum of solar wind fluctuations consists of several power-law spectra with different slopes over different scale ranges (Bruno & Carbone 2005, 2013). The largest scale range with a slope of -1 is the energy-containing scale that reflects the global inhomogeneity of the three-dimensional (3D) solar wind. In the next smaller range, the spectrum is often a power law of $-5/3$ that corresponds to that of Kolmogorov turbulence. This range is called the inertial range, and the break scale with the energy-containing range is called the "correlation length," and is a measure of the spatial scale of turbulent eddies (Zank et al. 1996). In the inertial range, the energy in fluctuations is transferred to smaller scales by a cascade process without energy dissipation. When the transfer of energy reaches the scale where dissipation by kinetic processes are dominant, the turbulent energy begins to be converted into thermal energy. Besides plasma heating, nonlinear turbulent processes associated with Reynolds stresses associated with turbulence are thought to contribute to the acceleration of the solar wind.

On the other hand, the characteristics of turbulence can be modified significantly by the large-scale distribution of the radial and lateral inhomogeneity of the global magnetic field and solar wind plasma parameters. Turbulence can be generated initially by convective motions in the photosphere and then transferred into the corona along magnetic field lines. The strongly inhomogeneous magnetic field of the Sun (in the corona and in the interplanetary space) leads to an inhomogeneous supply and transport of turbulence.

Turbulence in solar wind plasma can play essential roles in the heating of coronal (e.g., Tu 1988; Matthaeus et al. 1999a; Oughton et al. 2001) and solar wind (Matthaeus et al. 1999b; Smith et al. 2001; Adhikari et al. 2015a) plasma and the acceleration of the solar wind, as well as the acceleration of energetic particles associated with interplanetary shocks (Zank et al. 2000, 2007). The inhomogeneous deposition of turbulence energy results in an inhomogeneous solar wind speed. The inhomogeneity of the solar wind introduces expansion, shear, and mixing of solar wind plasma (Zank et al. 1996), which can enhance the production and evolution of turbulence. Turbulence can also be generated by energetic particles and shocks.

Because of the close coupling of turbulence, solar wind, and energetic particles, a comprehensive model describing not only turbulence but also the large-scale inhomogeneity of the solar wind and the IMF is necessary to understand the physics of these phenomena. The role of turbulence in solar coronal heating and solar wind acceleration is one of the challenging goals for the forthcoming Solar Orbiter and Solar Probe Plus space missions.

Many theoretical approaches have been introduced to study the transport and evolution of turbulence in the solar wind. Recently, Zank et al. (2012) proposed a nonlinear model describing the transport of MHD turbulence, introducing a closed set of six equations of six variables, three of which represent the turbulence intensity of forward and backward propagating modes and the residual energy, together with three corresponding correlation lengths. Adhikari et al. (2014, 2015a) developed a one-dimensional (1D) model reduction of the Zank et al. (2012) turbulence transport model and well-reproduced the observed turbulence. However, in their 1D model, Adhikari et al. (2014, 2015a) did not study the role that the inhomogeneous 3D global structure of solar wind and IMF can have on the transport and generation of turbulence.

In this paper, we present a 3D numerical model in which the large-scale MHD solar wind and turbulence transport therein are coupled, and investigate the effect of the inhomogeneous 3D structure of the background solar wind on the transport of turbulence. We assume a simple magnetic configuration with a tilted dipole to mimic solar minimum conditions. The model includes many effects, including inhomogeneity of the background solar wind and IMF, and diverse possible sources of turbulence. To separate the effect of each, we simulated intermediate comparative cases between a solar minimum condition and a 1D model similar to that used in Adhikari et al. (2015a). Based on this comparison, we discuss the connection between turbulence generation and the bimodal solar wind structure. The turbulence variables under solar minimum conditions are compared with those derived from in situ measurements made by *Helios* and *Ulysses*. Our intention with this work is to carefully and systematically extend our idealized 1D model to an idealized 3D model in an effort to understand the changes on the basic physics of turbulence transport in a more complex structured solar wind. We do not try to explain in great detail the relatively few existing observations of the heliospheric evolution of turbulence. However, we do use the observations that exist to try to determine whether the model presented here is in the right general direction. We do not attempt to tweak the model in any way to match observations.

In the following section, we describe our numerical models. Section 3 shows results from six test cases with spherically symmetric solar wind and Section 4 shows results from two non-asymmetric solar wind cases. The fully 3D solar wind cases are compared with results from in situ measurements in Section 5. Section 6 concludes with a Summary and Discussion.

2. Large-scale Heliospheric Model

Shiota et al. (2014) recently developed a 3D MHD model of the solar wind in the inner heliosphere, which is used in the present study. The model results are in reasonable agreement with in situ measurements of the solar wind at the orbits of Earth, Venus, and Mars (Shiota et al. 2014). This MHD model is now used as part of the real-time space weather forecast system SUSANOO[5] at Nagoya University. In this Section, we first briefly introduce the basic MHD model of the solar wind. After that, we introduce the theoretical turbulence transport model developed by Zank et al. (2012), which is now coupled into the solar wind MHD model.

[5] http://cidas.isee.nagoya-u.ac.jp/susanoo/

2.1. Solar Wind MHD Model

The solar wind MHD model of Shiota et al. (2014) calculates the spatial and temporal variation of the 3D solar wind on the basis of a time series of observed photospheric magnetic field synoptic maps. The inner heliosphere defined in the Heliographic Inertial (HGI) coordinate system is discretized with a Yinyang grid (Kageyama & Sato 2004). In the MHD model (Shiota et al. 2014), we integrate the following MHD equations:

$$\frac{\partial \rho}{\partial t} + \mathrm{div}(\rho \boldsymbol{v}) = 0, \tag{1}$$

$$\frac{\partial \rho \boldsymbol{v}}{\partial t} + \mathrm{div}(\rho \boldsymbol{v}\boldsymbol{v} - \boldsymbol{B}\boldsymbol{B} + p_T \boldsymbol{I}) = \rho \boldsymbol{g}, \tag{2}$$

$$\frac{\partial \boldsymbol{B}}{\partial t} + \mathrm{div}\,(\boldsymbol{B}\boldsymbol{v} - \boldsymbol{v}\boldsymbol{B} + \psi \boldsymbol{I}) = 0, \tag{3}$$

$$\frac{\partial e}{\partial t} + \mathrm{div}\,((e + p_T)\boldsymbol{v} - (\boldsymbol{v}\cdot\boldsymbol{B})\boldsymbol{B}) = \rho \boldsymbol{v}\cdot\boldsymbol{g} + H, \tag{4}$$

where $e = \frac{\rho v^2}{2} + \frac{p}{\gamma - 1} + \frac{B^2}{2}$, $\boldsymbol{g} = -\frac{GM}{r^3}\boldsymbol{r}$, and $p_T = p + \frac{B^2}{2}$. These equations are normalized with typical values: $L_0 = R_\odot = 6.96 \times 10^5$ km, $\tau_0 = 1$ h $= 3600$ s, $\rho_0 = 1\ \mathrm{cm}^{-3} \times m_\mathrm{H}$, $V_0 = L_0/\tau_0 = 193.3$ km/s, $B_0 = V_0 \times \sqrt{4\pi\rho_0} = 8.864$ nT, and $p_0 = 6.252 \times 10^{-2}$ nPa. $\boldsymbol{I}$ is the unit matrix in Cartesian coordinates. The additional variable ψ is integrated with the following equation

$$\frac{\partial \psi}{\partial t} + c_h^2\, \mathrm{div}\,\boldsymbol{B} + c_p \psi = 0, \tag{5}$$

that relieves the numerical deviation of the divergence free (solenoidal) condition of magnetic field (Dedner et al. 2002), where c_h and c_p are the propagation speed of ψ defined as the maximum characteristic speed within the numerical domain and the diffusion coefficient of ψ is defined as $c_p = c_h/0.18$, respectively (Dedner et al. 2002). m_H, G, and M are the proton mass, the gravitational constant, and the solar mass, respectively. H is a heating term (Adhikari et al. 2014, 2015a) that is discussed later and is set to be 0 in this study. These equations are solved using a finite volume method with a Harten–Lax–van Leer Discontinuities approximate Riemann solver (Miyoshi & Kusano 2005), which is combined with the third-order Monotone Upstream-centered Schemes for Conservation Laws and second-order Runge–Kutta time integration.

The numerical domain in this study is set as $60R_\odot \leqslant r \leqslant 1290R_\odot$ (6 au). The inner boundary conditions at $r = 60R_\odot$ are rotating and time-varying solar wind maps obtained from the 3D potential coronal magnetic field (Shiota et al. 2012) and empirical velocities between coronal magnetic field and solar wind parameters (Wang & Sheeley 1990; Totten et al. 1995; Arge & Pizzo 2000; Hayashi et al. 2003).

The solar wind 3D structure is determined from the time series of solar wind and IMF maps specified on the inner boundary of the MHD simulation (Shiota et al. 2014). In order to obtain a simple solar wind structure, we use two simplified steady magnetic field configurations:

1. a monopole field structure in which the field is outward-directed and its strength (0.55 G or 0.275 G at $r = 2.5\ R_\odot$) is spherically symmetric; and

2. a tilted dipole magnetic field whose magnetic axis is inclined at 30° from the rotational axis of the Sun.

Furthermore, we use two types of solar wind velocity maps:

1. a spherically symmetric solar wind flow with a constant speed 400 km s^{-1} or 600 km s^{-1}; and
2. a bimodal (fast and slow) solar wind flow whose speed is determined from the tilted dipole potential field and the Wang–Sheeley–Arge 2000 formula (Wang & Sheeley 1990; Arge & Pizzo 2000).

We ran the simulations for a sufficiently long time, so that a steady-state solution was obtained. We show numerical results with combinations of the four configurations and compare with observations of turbulence in the solar wind.

2.2. Turbulence Transport Model

We combine the theoretical turbulence transport model developed by Zank et al. (2012) with our global MHD model (Shiota et al. 2014). In general, turbulence in the MHD regime can be treated with the MHD equations, Equations (1)–(4), if the spatial resolution of the numerical simulation is sufficiently high to resolve the higher wavenumber turbulence. However, it is difficult, if not impossible currently, to solve a global MHD simulation with such a high spatial resolution because the energy-containing rage of the MHD turbulence is too large. We separate the high frequency fluctuations in the velocity $\boldsymbol{v}$ and magnetic field $\boldsymbol{B}$ (Zhou & Matthaeus 1990), which cannot be described by the global MHD simulation, and denote the scale-separated fluctuations as $\boldsymbol{u}$ and $\boldsymbol{b}$. The fluctuations in solar wind velocity and magnetic field associated with oppositely propagating Alfvén modes are described by the Elsässar variables (Elsässer 1950):

$$\boldsymbol{z}^{\pm} = \boldsymbol{u} \pm \boldsymbol{b}/\sqrt{4\pi\rho}. \tag{6}$$

The transport and modulation of the Elsässar variables are described by scale-separated incompressible MHD equations (Marsch & Tu 1989, 1990; Zhou & Matthaeus 1990):

$$\frac{\partial \boldsymbol{z}^{\pm}}{\partial t} + (\boldsymbol{U} \mp \boldsymbol{V}_A)\cdot\nabla\boldsymbol{z}^{\pm} + \frac{1}{2}\nabla\cdot(\boldsymbol{U}/2 \pm \boldsymbol{V}_A)\boldsymbol{z}^{\pm} + \boldsymbol{z}^{\mp}\cdot\left[\nabla\boldsymbol{U} \pm \frac{\nabla\boldsymbol{B}}{\sqrt{4\pi\rho}} - \frac{\boldsymbol{I}}{2}\nabla\cdot(\boldsymbol{U}/2 \pm \boldsymbol{V}_A)\right] = \boldsymbol{N}\boldsymbol{L}_{\pm} + \boldsymbol{S}^{\pm} \tag{7}$$

where U is the mean velocity, V_A is the mean Alfvén velocity, $\boldsymbol{N}\boldsymbol{L}_{\pm}$ are nonlinear dissipation terms, and $\boldsymbol{S}^{\pm}$ are source terms for the turbulence. The detail of the source terms $\boldsymbol{S}^{\pm}$ are described in the next subsection.

Equation (7) is derived from the standard incompressible reduction of the MHD Equations (1)–(4). Strictly speaking Equation (7) is therefore valid only for solar wind conditions satisfying $\beta_p \gg 1$, where β_p is the usual plasma beta (Zank & Matthaeus 1991; Hunana & Zank 2010). Despite this limitation, the turbulence models (Zank et al. 1996, 2012; Matthaeus et al. 1999b; Smith et al. 2001; Adhikari et al. 2014, 2015a) derived from it are quite well validated by in situ observations of low-frequency turbulence in the solar wind (Adhikari et al. 2014, 2015a).

The turbulence transport model of Zank et al. (2012) considered the temporal and spatial evolution of three moments of the small-scale fluctuations (unit: energy per unit mass),

$$f \equiv \langle z^{+2}\rangle = \langle \boldsymbol{z}^{+}\cdot\boldsymbol{z}^{+}\rangle, \tag{8}$$

$$g \equiv \langle z^{-2}\rangle = \langle \boldsymbol{z}^{-}\cdot\boldsymbol{z}^{-}\rangle, \tag{9}$$

and

$$E_D \equiv \langle \boldsymbol{z}^{+}\cdot\boldsymbol{z}^{-}\rangle = \langle u^2\rangle - \langle b^2/4\pi\rho\rangle. \tag{10}$$

The transport equations of these variables are derived by taking moments of Equation (7), corresponding to Equations (42)–(44) of Zank et al. (2012):

$$\frac{\partial f}{\partial t} = -(\boldsymbol{U} - \boldsymbol{V}_A)\cdot\nabla f - \nabla\cdot\left(\frac{\boldsymbol{U}}{2} + \boldsymbol{V}_A\right)f + M^{+}E_D - 2\frac{f^2\sqrt{g}}{L^{+}} + 2S^{+}; \tag{11}$$

$$\frac{\partial g}{\partial t} = -(\boldsymbol{U} + \boldsymbol{V}_A)\cdot\nabla g - \nabla\cdot\left(\frac{\boldsymbol{U}}{2} - \boldsymbol{V}_A\right)g + M^{-}E_D - 2\frac{g^2\sqrt{f}}{L^{-}} + 2S^{-}; \tag{12}$$

$$\frac{\partial E_D}{\partial t} = -\boldsymbol{U}\cdot\nabla E_D - \frac{\nabla\cdot\boldsymbol{U}}{2}E_D + \frac{M^{-}}{2}f + \frac{M^{+}}{2}g - \frac{1}{2}\left(\sqrt{\frac{f}{g}}\boldsymbol{V}_A\cdot\nabla g - \sqrt{\frac{g}{f}}\boldsymbol{V}_A\cdot\nabla f\right) - \left[\frac{g\sqrt{f}}{L^{-}} - \frac{f\sqrt{g}}{L^{+}}\right]E_D + 2S_D, \tag{13}$$

where

$$M^{\pm} = \nabla\cdot\left(\frac{\boldsymbol{U}}{2} \pm \boldsymbol{V}_A\right) - 2\left(a\left[\nabla\cdot\boldsymbol{U} - \frac{(\boldsymbol{B}\cdot\nabla\boldsymbol{U})}{B^2}\cdot\boldsymbol{B}\right] \pm b\left[\nabla\cdot\boldsymbol{V}_A - \frac{\boldsymbol{B}\cdot\nabla|V_A|}{|B|}\right]\right) \tag{14}$$

and $L^{\pm}$ and L^{D} are variables related to the correlation lengths ($\lambda_{\pm}$ and λ_D) of these three moments, respectively. They are defined as $L^{+} \equiv f\lambda_{+}$, $L^{-} \equiv g\lambda_{-}$, and $L^{D} \equiv E_D\lambda_D$. In the turbulence transport model (Equations (11)–(13)), we solve simultaneously for the temporal and spatial evolution of the three variables $L^{\pm}$ and L^{D},

$$\frac{\partial L^{\pm}}{\partial t} = -(\boldsymbol{U} \mp \boldsymbol{V}_A)\cdot\nabla L^{\pm} - \nabla\cdot\left(\frac{\boldsymbol{U}}{2} \pm \boldsymbol{V}_A\right)L^{\pm} + \frac{M^{\pm}}{2}L_D; \tag{15}$$

$$\frac{\partial L^{D}}{\partial t} = -\boldsymbol{U}\cdot\nabla L^{D} - \frac{\nabla\cdot\boldsymbol{U}}{2}L^{D} + M^{-}L^{+} + M^{+}L^{-} - \left(\sqrt{\frac{L^{+}}{L^{-}}}\boldsymbol{V}_A\cdot\nabla L^{-} - \sqrt{\frac{L^{-}}{L^{+}}}\boldsymbol{V}_A\cdot\nabla L^{+}\right), \tag{16}$$

also derived from Equation (7). According to the derivation in Appendix A, the parameters a and b in Equation (14) are set to

$a = b = 1/2$ in the present study, which yields

$$M^{\pm} = \nabla \cdot \left(\frac{\boldsymbol{U}}{2} \pm \boldsymbol{V}_A\right) - \left[\nabla \cdot \boldsymbol{U} - \frac{(\boldsymbol{B} \cdot \nabla \boldsymbol{U})}{B^2} \cdot \boldsymbol{B}\right] \mp \left[\nabla \cdot \boldsymbol{V}_A - \frac{\boldsymbol{B} \cdot \nabla |V_A|}{|B|}\right] = -\nabla \cdot \left(\frac{\boldsymbol{U}}{2}\right) + \frac{(\boldsymbol{B} \cdot \nabla \boldsymbol{U})}{B^2} \cdot \boldsymbol{B} \pm \frac{\boldsymbol{B} \cdot \nabla |V_A|}{|B|}. \quad (17)$$

The model Equations (11)–(13), (15), and (16) are coupled to our 3D MHD model, utilizing the inhomogeneous solar wind $\boldsymbol{U}$ and $\boldsymbol{V}_A$ obtained from the MHD simulation, i.e., we solve the temporal variation of eight MHD variables and six turbulence variables simultaneously in the coupled model.

We note that related approaches have been introduced by Usmanov et al. (2000, 2011, 2014) and Kryukov et al. (2012). However, these authors coupled the much simpler turbulent transport models of Zank et al. (1996) and Breech et al. (2008) to 3D MHD models of the heliosphere. The Usmanov et al. (2014) and Kryukov et al. (2012) 3D MHD models included the back reaction of the turbulence on the global MHD flow by including both heating and Reynolds-averaged turbulence terms in the MHD model. This will be an important next step in the further development of our approach.

The coupling of turbulence and heating by dissipation of the turbulence using a 1D Zank et al. (2012) model was investigated by Adhikari et al. (2015a), The intensities of inward and outward propagating turbulence show a large asymmetry in fast solar wind streams, whereas they are comparable in slow solar wind streams.

Although these are coupled with each other, in this study, we show results in a steady state with coupling in one direction only (no source term, $H = 0$ in Equation (4)).

2.3. Sources of Turbulence

The origin of the three turbulence intensities described in the previous section depend on the assumed inner boundary conditions of the simulation and the generation of turbulence by various sources within the numerical domain.

2.3.1. Boundary Condition

We consider the turbulent energy densities g and f to be associated with forward and backward propagating modes, respectively. The propagation direction in the radial direction depends on the sign of the IMF radial component. If we used actual directional inhomogeneous magnetic field data, the boundary condition would have to be specified taking into account the IMF direction. However, the development of such a technique is beyond of the scope of this paper, and we specify instead spherically symmetric values on the inner boundary, which are slightly modified from those used in Adhikari et al. (2015a), as listed in Table 1.

To examine if the boundary conditions are inappropriate, we performed simulations with the turbulence boundary conditions with forward and backward propagating modes swapped (g, f, $\lambda_{\pm}$). The parameters for each case are tabulated in Table 2. We denote the cases where $g = g_0$, $f = f_0$, $\lambda_+ = \lambda_{+0}$, and $\lambda_- = \lambda_{-0}$, as "proper" in Table 2. The swapped cases, where $g = f_0$, $f = g_0$, $\lambda_+ = \lambda_{-0}$, and $\lambda_- = \lambda_{+0}$, are denoted as "opposite."

Table 1
Turbulence Variables on the Inner Boundary (Same as in Adhikari et al. 2015a)

Name	symbol	values	unit
Strength of outward propagating mode	g_0	14,000	$(\mathrm{km\ s^{-1}})^2$
Strength of inward propagating mode	f_0	268	$(\mathrm{km\ s^{-1}})^2$
Strength of Residual energy	E_{D0}	−57.07	$(\mathrm{km\ s^{-1}})^2$
Correlation length of outward propagating mode	λ_{-0}	1.16×10^5	km
Correlation length of inward propagating mode	λ_{+0}	2.14×10^5	km
Correlation length of residual energy	λ_{D0}	3.05×10^6	km

Table 2
Parameter List of the Numerical Results

Case	Boundary	Solar wind		IMF	Turbulence
	condition	Structure	V_{SW} [km s^{-1}]	Structure	source term
Case 1	proper	1D	600	Monopole	Yes
Case 2	proper	1D	400	Monopole	Yes
Case 3	proper	1D	600	Monopole, $\times 1/2$	Yes
Case 4a	proper	1D	600	Monopole	No
Case 4b	proper	1D	600	Monopole	Yes, $\times 2$
Case 5	opposite	1D	600	Monopole	Yes
Case 6	proper	Bimodal		Monopole	Yes
Case 7a	proper	Bimodal		Dipole	Yes
Case 7b	opposite	Bimodal		Dipole	Yes
Case 8a	proper	Bimodal		Dipole	Yes, $\times 2$
Case 8b	opposite	Bimodal		Dipole	Yes, $\times 2$

2.3.2. Source Terms

We applied only one form of turbulence source terms, which is that associated with the generation of shear at the interface of fast and slow solar wind streams (Coleman 1968; Roberts et al. 1987, 1992; Zank et al. 1996; Adhikari et al. 2015a). Roberts et al. (1987) investigated observationally the origin and evolution of fluctuations in the solar wind using the *Helios* and Voyager spacecraft data sets and observed rapid evolution of the normalized cross-helicity in the inner heliosphere, which is indicative of strong in situ nonlinear dynamical processes, i.e., the shear of the streams. Zank et al. (1996) modeled this process with a velocity shear source term in the form of $C\Delta U \langle z^2 \rangle / r$ though the generation of turbulence by stream shear should be independent of intensities of the background turbulence. Therefore, we apply the source terms for solar wind turbulence, which are extensively studied elsewhere (Zank et al. 2017). We constructed dimensionally new source terms parameterized based on $(\mathrm{velocity})^3/\mathrm{length} \sim (\mathrm{velocity})^2/\mathrm{time}$. The way we chose the $(\mathrm{velocity})^3$ term was to combine the two characteristic speeds, viz., the Alfvén speed and the speed of fluctuations. We find that the combination $V_A^2 \Delta U$ seems to work best where $\Delta U \sim 5$–10 km s^{-1} is of the order of the characteristic speed of velocity fluctuations. We could have written the source term in e.g., Equation (11) as Constant $\times \Delta U V_A^2 r_0 / r^2 = C_+ V_A^2 r_0 / r^2$. The dimension of C_+ and C_- is that of velocity. We use the following modified 1D model

$$S^+ = \frac{C_+ V_{A0}^2 r_0}{r^2}; \quad (18)$$

$$S^- = \frac{C_- V_{A0}^2 r_0}{r^2}; \quad (19)$$

$$S_D = -\frac{S^+ + S^-}{4}, \quad (20)$$

where $V_{A0} = 174.4$ km s^{-1}, $r_0 = 62.35 R_\odot$, $C_+ = 2.00 V_0$ km s^{-1}, and $C_- = 0.80 V_0$ km s^{-1}. These forms were chosen to ensure consistency of the model and observed values of the various turbulence quantities. To examine the effect of the source terms, we consider cases in which the sources are set to $C_\pm = 0$ or two times stronger than shown above. These cases are denoted as "No" or "×2" in the last column of Table 2, respectively.

Since we consider only solar minimum conditions, source terms associated with the generation of turbulence by shock waves (Zank et al. 1996; Adhikari et al. 2015a) are neglected. Similarly since the simulated domain is restricted to within 6 au, pickup ion driven turbulence (Lee & Ip 1987; Williams & Zank 1994; Zank et al. 1996) is neglected too.

3. Results

The numerical results for eight comparative cases are shown in the present paper. First, the basic case results are shown in detail in Section 3.1. Comparisons of five spherically symmetric solar wind cases to the basic case are shown in the following sections.

3.1. Basic Axisymmetric Case

First, for the Basic Case (Case 1), we assumed a spherically symmetric solar wind flow of 600 km s^{-1} at the inner boundary (60 $R_\odot$) and a monopole IMF with magnetic field strength is 0.55 G at source surface 2.5 $R_\odot$. The radial field in the magnetic field vector becomes $B_r = 7.43$ nT at 1 au, which is a comparable value to that observed in situ (Adhikari et al. 2015a).

Figure 1 shows two-dimensional distributions of velocity (panel (a)), magnetic field (panel (b)), magnetic field alignment to the radial direction (panel (c)), and turbulence variables (panel (d)–(i)) in the meridional plane in the HGI coordinate. In spite of the spherically symmetric boundary conditions, the steady state shows latitudinal distributions resulting from the rotation of the Sun (the inner boundary), i.e., forming the Parker spiral IMF (Parker 1958; see Figure 1(c)). V_r and B_r have spherically symmetric distributions, while the magnetic field alignment $|B_r|/|B|$ has a cylindrically symmetric distribution. Because of the inhomogeneous distribution of the background solar wind and IMF, the distributions of turbulence intensities and correlation lengths have latitudinal dependences (Figures 1(d)–(i)).

For a quantitative comparison between the four different latitudes, we use the 1D radial plots of the background solar wind, IMF, and the turbulent variables in Figure 2. The different colors in each radial plot correspond to different latitudes (0° (black), 30° (blue), 60° (green), and 90° (red)). Figures 2(a) and (b) show the solar wind speed and IMF along the four different latitude lines, respectively. The profiles of the solar wind speed and the IMF radial component are identical due to the spherically symmetric distribution seen in Figure 1, while only the IMF azimuthal component has different distribution.

Figure 2(e) shows radial plots of the three turbulence strengths: the solid lines denote g, the dashed lines f, and the dotted lines $-E_D$. For the outward propagating intensity g, the distributions are similar and small differences can be seen beyond 2 au. In contrast, the profiles of the other two intensities show a stronger dependence with latitude, with the lower latitude profiles showing a greater decrease at larger distances. From Figure 1(d), since the contours of the distribution f seem to be more vertically oblate with distance from the Sun, the distribution will approach a cylindrical distribution, and the transport of the inward propagating intensity f is likely to depend on the direction of IMF (Figure 1 (c)) in these regions.

From the turbulence transport Equations (11)–(13), (15), and (16), the dependence on the magnetic field alignment $|B_r|/|B|$ appears only in the mixing term as shown in Equation (17). For large distances, Equation (17) can be reduced as

$$M^\pm \sim -\nabla \cdot \left(\frac{\boldsymbol{U}}{2}\right) + \frac{B_r^2}{B^2}\frac{\partial U_r}{\partial r} + \frac{B_\theta^2 + B_\phi^2}{B^2}\frac{U_r}{r} \sim -\frac{B_r^2}{B^2}\frac{U_r}{r}, \quad (21)$$

assuming that $\boldsymbol{U} \sim U_r \boldsymbol{e}_r$ and $V_A \ll U_r$. This indicates that mixing of the inward and outward propagating modes and the residual energy can be the relatively dominant factor in determining the backward propagating mode intensity in the distant region. The terms that include the mixing in Equations (11) and (12) are positive because E_D is negative. In the low latitude region, the term approaches 0 and hence the absence of mixing results in lower intensities.

Figures 2(c) and (d) show the normalized cross-helicity (solid), residual energy (dashed), and Alfvén ratio (Bruno et al. 2007), respectively,

$$\sigma_C = \frac{g - f}{g + f} \times \frac{B_r}{|B_r|}; \quad (22)$$

$$\sigma_D = \frac{2E_D}{g + f}; \quad (23)$$

$$r_A = \frac{g + f + 2E_D}{g + f - 2E_D}. \quad (24)$$

Corresponding to the latitudinal dependence seen in Figure 2(e), these three parameters reflect the same latitudinal dependence.

Notice too that the decay of the normalized residual energy σ_D indicates that the turbulence is becoming increasingly dominated by the magnetic field fluctuations (see Adhikari et al. 2015a, 2015b) rather than the kinetic energy. In the inner region, the dominance of the outward propagating turbulence intensity relative to the other two intensities (Figure 2(e)) reflects that the normalized cross-helicity is nearly equal to +1 and that the normalized residual energy is ∼0. The normalized residual energy approaches approximately −0.5 as the intensity of the residual energy becomes half of the average of the inward and outward propagating turbulence in the outer regions (Figure 2(e)). This is reflected in the Alfvén ratio plot r_A, which approaches ∼0.3 (Figure 2(d)). The normalized cross-helicity approaches ∼0.5 as the intensity of the inward propagating turbulence becomes half that of the outward propagating turbulence. The reductions in the intensities of the inward propagating turbulence and the residual energy in lower latitudes results in the difference in the radial profiles of σ_C, σ_D, and r_A (Figures 2(c) and (d)).

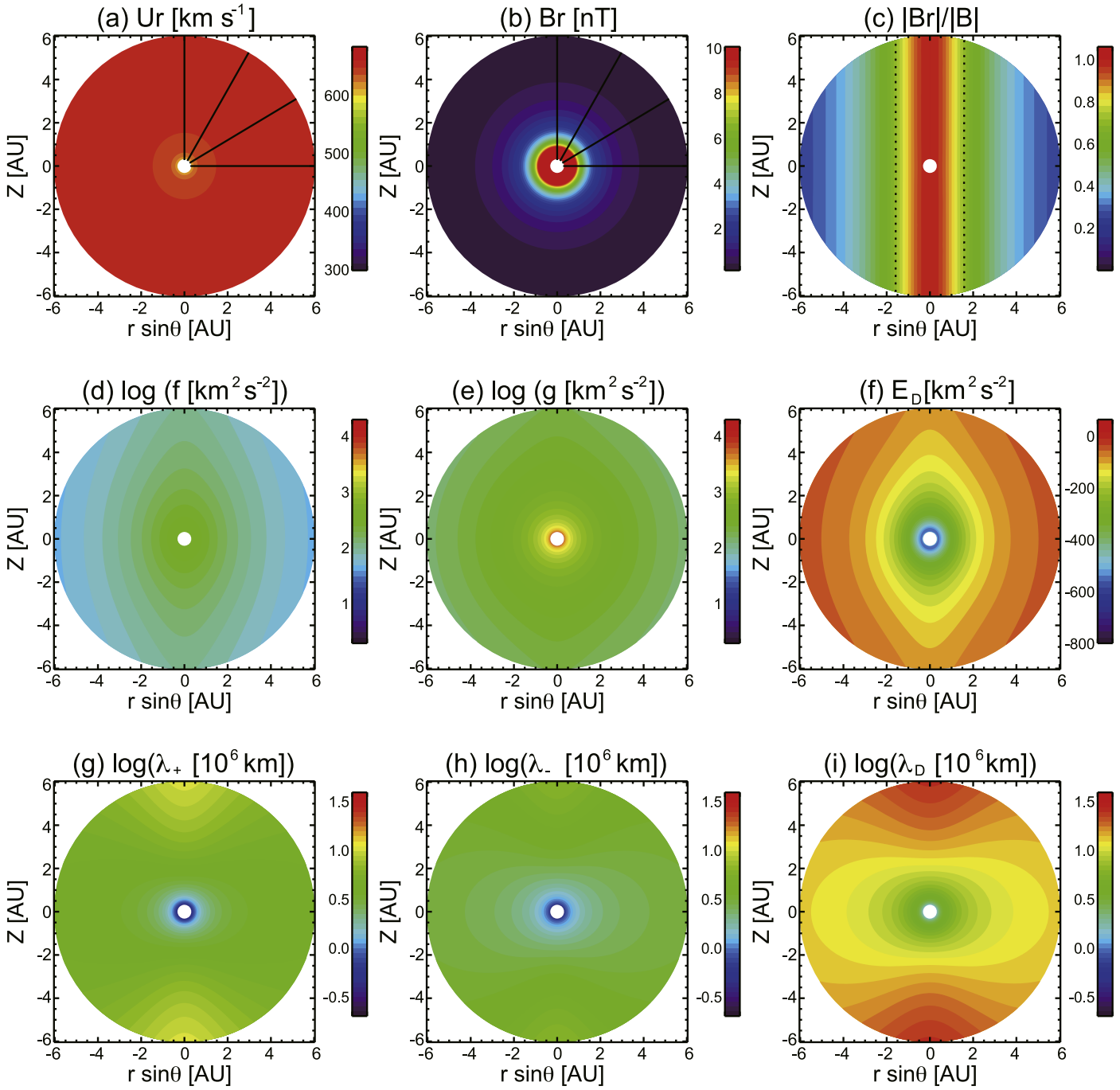

Figure 1. Panels (a)–(i) are 2D plots of the radial components of velocity, IMF radial component, and alignment of the IMF to the radial direction, and three turbulence intensities and correlation lengths in the meridional plane in Case 1, respectively. In Panels (a) and (b), four solid lines display the four latitudes (0°, 30°, 60°, 90°), along which 1D profiles are drawn in Figure 2. The dotted line in Panel (c) shows the position where $|B_r|/|B| = 1/\sqrt{2}$ i.e., $|B_r| = |B_\phi|$.

Figure 2(f) shows radial plots of the three turbulence correlation lengths: the solid lines denote λ_-, the dashed lines λ_+, and the dotted lines λ_D. The distributions of all the correlation lengths show a similar latitudinal dependence.

The line in each panel of Figure 3 show the radial profiles in the equatorial plane (solid lines) and over the poles (dotted lines) for all the variables. Observed values (Adhikari et al. 2015a) for the three strengths are overlaid using the cross symbols in Panels (d), (e), (g), (h), and (i) for reference. A word of caution is appropriate about the observational data overplotted on the panels of the radial plots. As discussed at length in Adhikari et al. (2015a, 2015b), the observations combine *Helios* data from 0.29 au to 0.9 au and *Ulysses* data 1.3–4.8 au. The data, taken during solar minimum conditions, is nonetheless from different decades, used different instrumentation, and is a combination of in-ecliptic and out-of-ecliptic solar wind data. During the periods of observation, the IMF was approximately radial. Despite these caveats, the observed turbulence properties appear to provide a reasonable quantification of the evolution of various turbulence parameters from 0.29 to ∼5 au, and is in reasonable in accordance with the theoretical model of Adhikari et al. (2015a, 2015b).

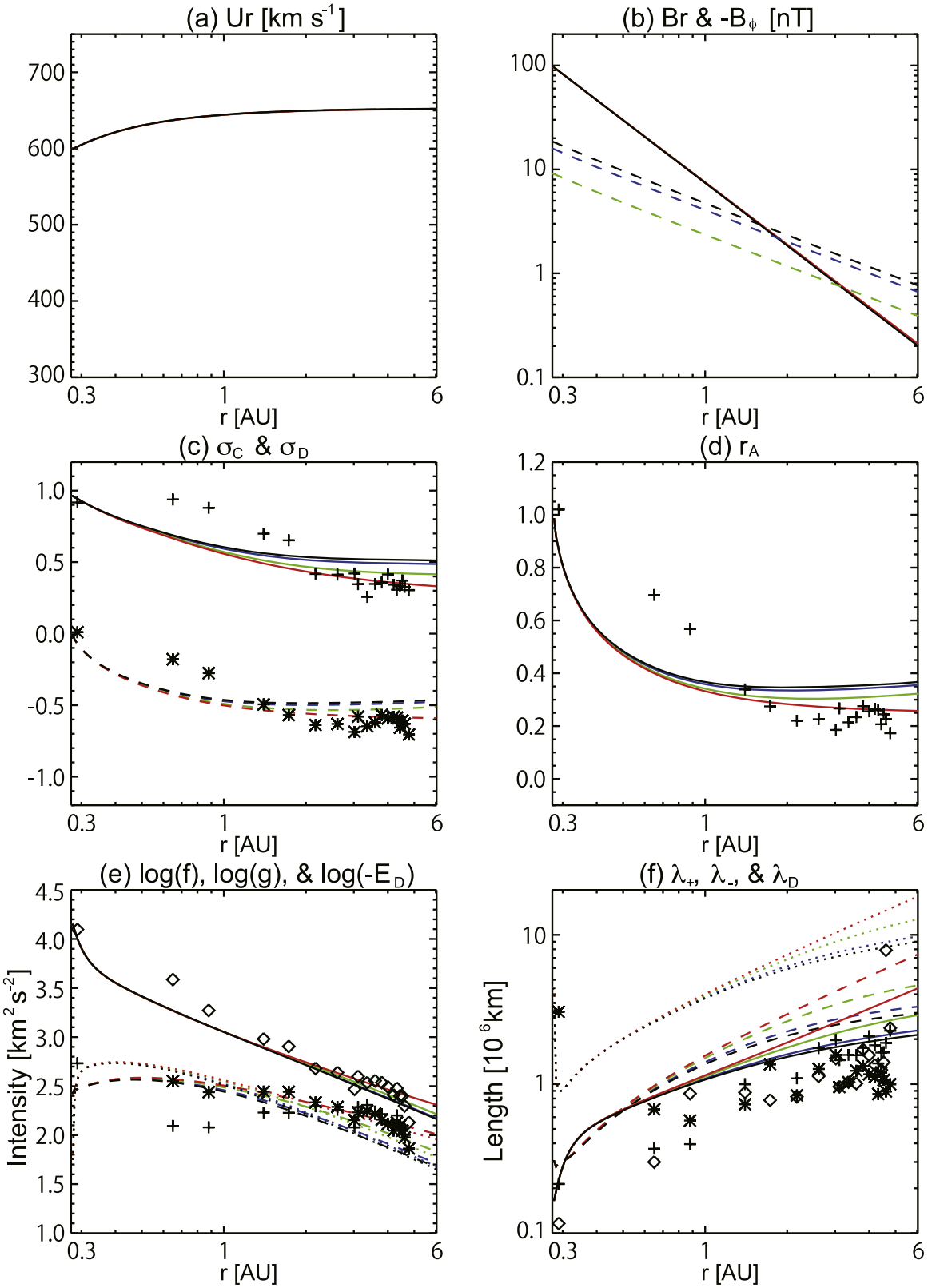

Figure 2. 1D plots along four different latitudes (0° (black), 30° (blue), 60° (green), and 90° (red)) for Case 1. Observed values of turbulent intensities and normalized ones Adhikari et al. (2015a) are overplotted in panels (c)–(f). Panel (a) shows radial profiles of solar wind speed. Panel (b) shows radial profiles of the radial component (solid lines) and the azimuthal component (dashed lines) of the IMF. Panel (c) shows normalized cross-helicity (solid lines) and normalized residual energy (dashed lines). Panel (d) shows radial profiles of the Alfvén ratio. Panel (e) shows the forward (solid lines) and the backward (dashed lines) propagating intensities and residual energy (dotted lines). Radial profiles of the corresponding correlation lengths are shown in Panel (f).

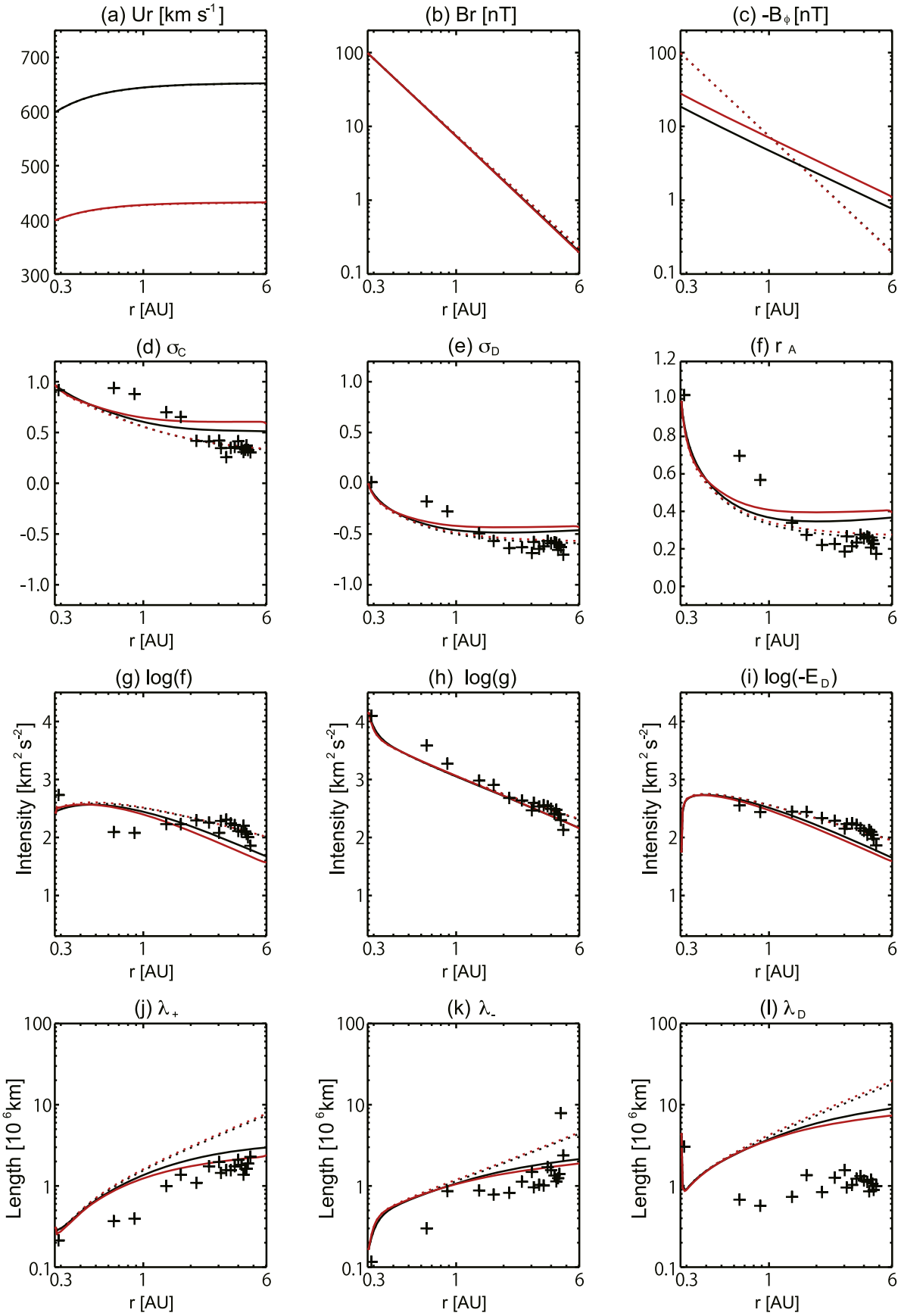

Figure 3. Comparison between Case 1 (black) and Case 2 (red). Solid line of each color in each panel displays a 1D radial plot along the equatorial line (lat. = 0°), while the dotted lines show that along the pole (lat. = 90°).

3.2. Effect of Solar Wind Speed Boundary Conditions

Case 2 differs from Case 1 in that the solar wind speed is reduced to 400 km s^{-1} from the 600 km s^{-1} of Case 1. Since the behavior of the global distributions is similar to those in Case 1, only radial profiles along the equatorial line and over the poles are compared, as shown with red lines in Figure 3 to illustrate the latitudinal dependence.

The main differences are in the speed (Figure 3(a)) and hence in the IMF because of the Parker spiral, as shown in Figure 3(c). The azimuthal component in Case 2 at the equator is 1.5 times larger than that in Case 1.

A comparison of the turbulence intensities is shown in Figures 3(g)–(i). The profiles of the three turbulence intensities along the pole (dotted lines in the panels) are almost identical. This means that the advection of the turbulence in the completely radial magnetic field does not introduce any differences.

In the equatorial plane, the inward propagating mode intensity is smaller than that of Case 1, intensity is larger than that of Case 1, while that of outward propagating modes is almost identical. These different trends can be understood from the terms related to the Alfvén velocity in Equation (17), i.e., the term including b in Equation (14), since the relative amplitude of $\boldsymbol{V}_A$ and its gradient relative to $\boldsymbol{U}$ are larger in Case 2 than in Case 1. Therefore, the difference between inward and outward propagating modes, i.e., cross-helicity, tends to be amplified (see Figure 3(d)) with the heliocentric distance. This is a consequence of the difference in the Parker spiral of IMF between the two cases, since the magnetic field alignment $|B_r|/|B|$ decreases faster in Case 2. This effect can suppress the mixing of turbulence in the inner region compared to Case 1.

From observations, it is known that for turbulence in the slow solar wind is balanced, having the same amplitude for inward and outward propagating modes. Thus, cross-helicity should be around zero. However, the results of our model with slow wind show a non-zero cross-helicity distribution. This can be caused by the use of inappropriate boundary values for the three turbulence intensities and corresponding correlation lengths. Although an improvement of the values for the slow solar wind is needed for more realistic studies, this is beyond the scope of the current study.

3.3. Effect of IMF Strength

Case 3 differs from Case 1 in that a different IMF strength is assumed, where the strength is reduced to half that of Case 1. The comparison of the radial profiles to Case 1 is shown in Figure 4. Because the solar wind speed is the same as in Case 1, the shape of the Parker spiral is identical (the ratio between the azimuthal and radial components seen in Figure 4(c)). Hence the mixing terms related to the magnetic field alignment are the same while the terms related to the amplitude of Alfvén velocity (namely $\nabla \cdot \boldsymbol{V}_A$) are halved.

The difference in the turbulence intensities is slight, though they can be seen at both the equator and the pole. This can be understood as the effect of an Alfvén velocity that is relatively small in the high-speed solar wind (Case 3).

3.4. Effect of a Source of Turbulence

Cases 4a (Figure 5) and 4b (Figure 6) are comparative cases to show that the source term (Zank et al. 1996; Adhikari et al. 2015a) is necessary to reproduce quantitatively the radial profiles of both inward and outward propagating turbulence. Case 4a neglects the source terms and Case 4b assumes source terms two times larger than those of Case 1, while the solar wind and IMF are identical to those in Case 1.

All three turbulence intensities in Case 4a (Figure 5) are reduced compared to those of Case 1 and the reduction in amplitudes is approximately similar (> a factor of five smaller) at both the equator and the pole. The radial dependence of the intensities also differs from those observed. Corresponding to the reduction in intensity, all the correlation lengths are ∼5 times longer. Because the relative amplitudes are different in their intensities, the difference in normalized cross-helicity σ_C and residual energy σ_D is not so different compared to the difference in turbulent intensities.

In contrast to Case 4a, all the turbulence intensities in Case 4b (Figure 6) are increased by a factor of about 1.5 compared to those of Case 1. Corresponding to the increase in the intensities, the correlation lengths are reduced by the same factor. That increase by a factor of ∼1.5, which is smaller than the factor of the source terms, can be understood as the increase in the nonlinear dissipation caused by the shorter correlation lengths. The radial profiles of the turbulence intensities in Case 4b show good agreement with the observed radial profiles (Figures 6(g), (h), and (i)).

In both Cases 4a and 4b, the increase (decrease) in the turbulence intensities is inversely related to the corresponding correlation lengths. This can be interpreted as follows. In our numerical models, the time variation of the correlation variables $L^{\pm}$ and L^D are solved using Equations (15) and (16). Because the background solar wind and IMF and the boundary conditions of the correlation variables $L^{\pm}$ and L^D are identical to those in Case 1, the distributions for $L^{\pm}$ and L^D are also identical. In contrast to $L^{\pm}$ and L^D, the turbulence intensities are different reflecting the difference in the source terms. Because the correlation lengths are obtained by dividing the correlation variables by the intensities (i.e., $\lambda^{+} = L^{+}/f$, $\lambda^{-} = L^{-}/g$, $\lambda^D = L^D/E_D$) , they are inversely related to the turbulence intensities.

3.5. Effect of Boundary Conditions on Turbulence

Case 5 (Figure 7) is one for which the inner boundary conditions of the inward and outward propagating modes (f and g) and corresponding correlation variables ($L^{\pm}$) are swapped as well as the source term ($S_{\pm}$). Because of the dominance of the inward propagating mode, the cross-helicity has negative values. The increase of residual energy in vicinity of the inner boundary is suppressed at both the equator and the pole. This indicates that the energy density in the inward and outward propagating modes in Case 5 is more inefficiently converted to the residual energy than in Case 1, i.e., more energy is dissipated through the nonlinear terms. The turbulence intensity of each dominant mode (f in Case 5) at $r = 6$ au is smaller by a factor of >1.5 than g in Case 1 in both the equatorial plane and over the pole.

The radial intensity profiles of inward (f) and outward (g) propagating modes and the residual energy (E_D) finally converge to the same value of ∼100 km^2 s^{-2} at the poles (red dotted lines in Figures 7(g)–(i)) at $r = 6$ au. This indicates that the turbulence over the pole is similar isotopically to that observed in the slow solar wind. In contrast to the pole, in the equatorial plane, the intensity of the dominant (inward propagating) mode f is a factor of 1.5 times higher than that

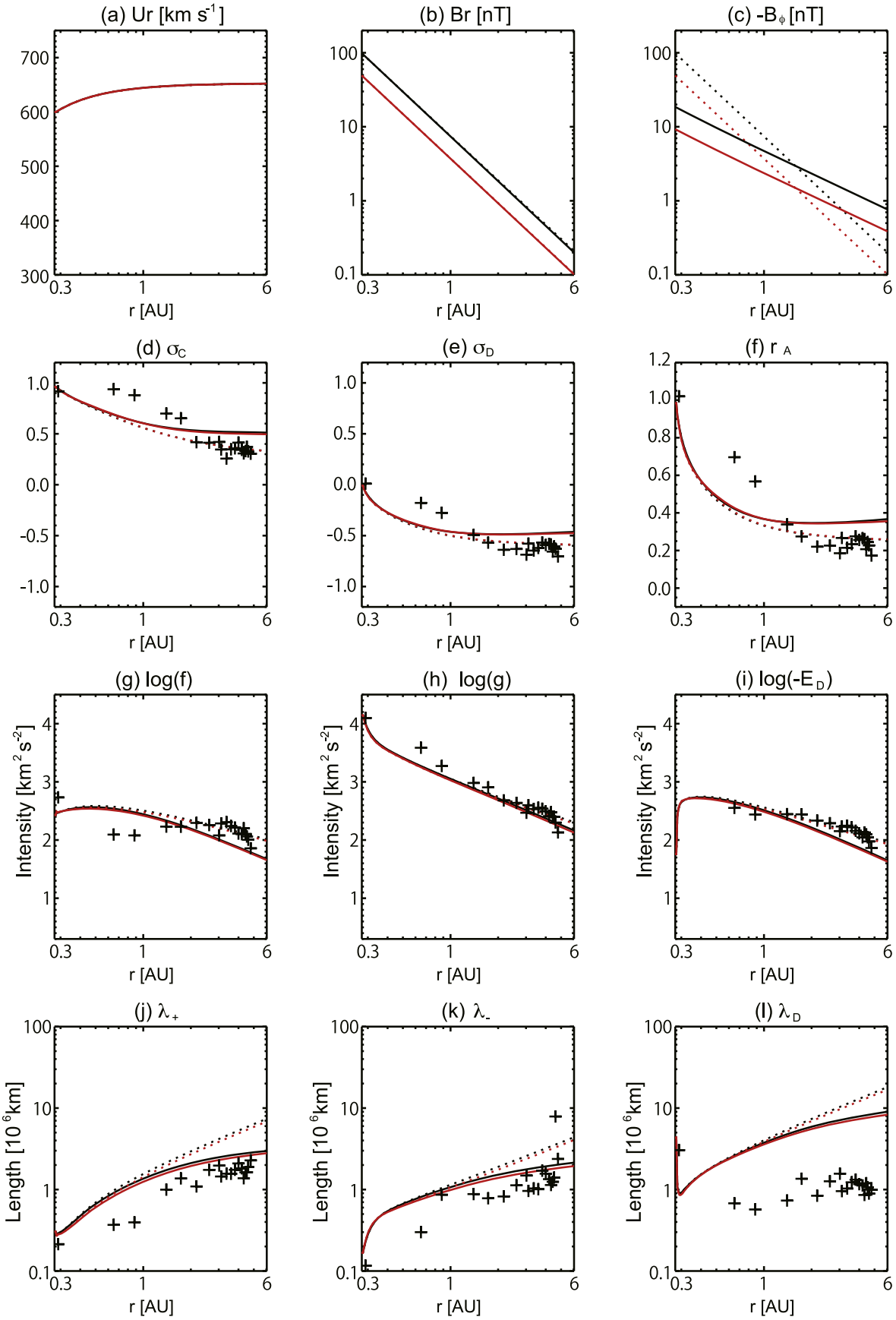

Figure 4. Comparison between Case 1 (black) and Case 3 (red). The format is the same as in Figure 3.

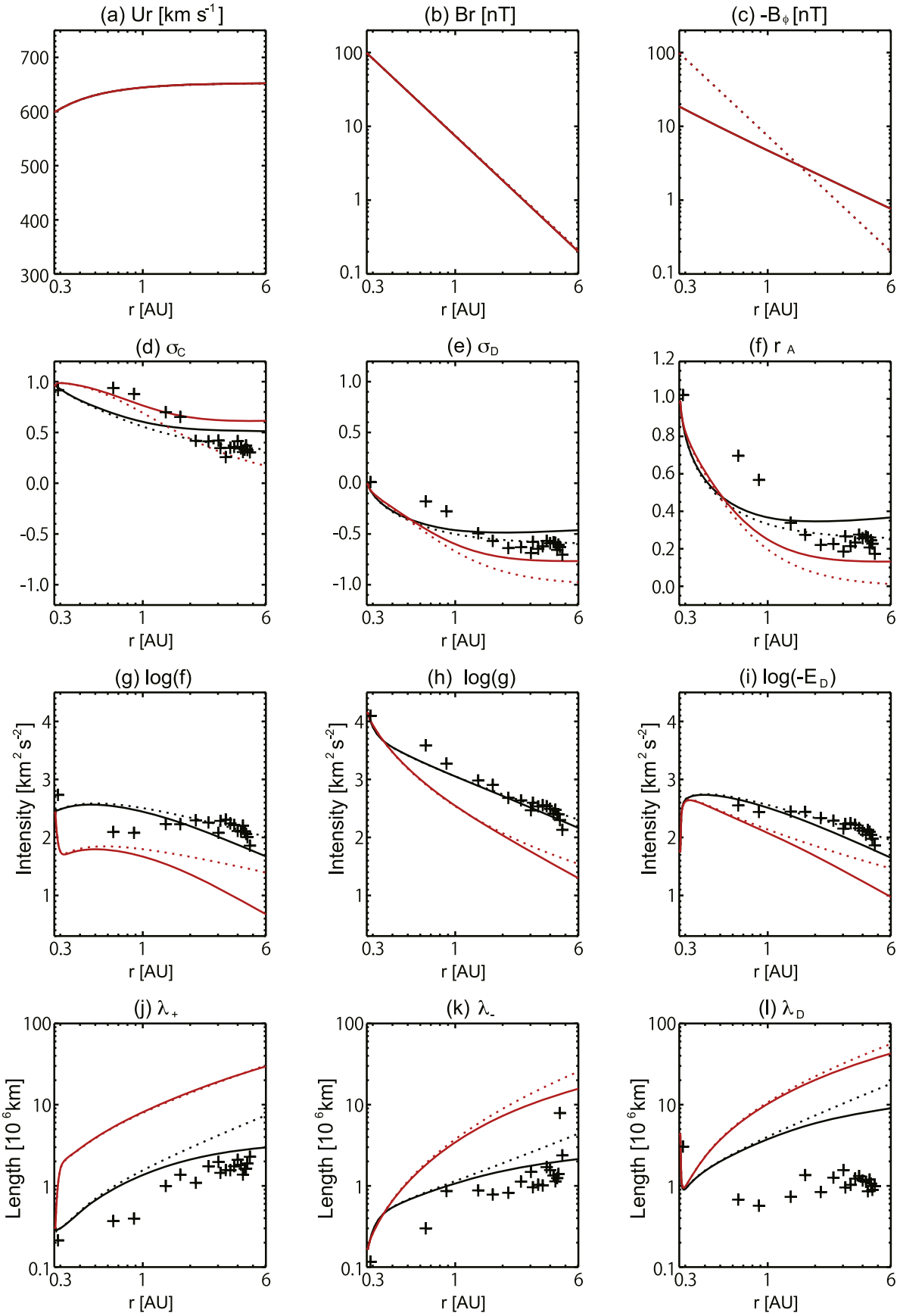

Figure 5. Comparison between Case 1 (black) and Case 4a (red). The format is the same as in Figure 3.

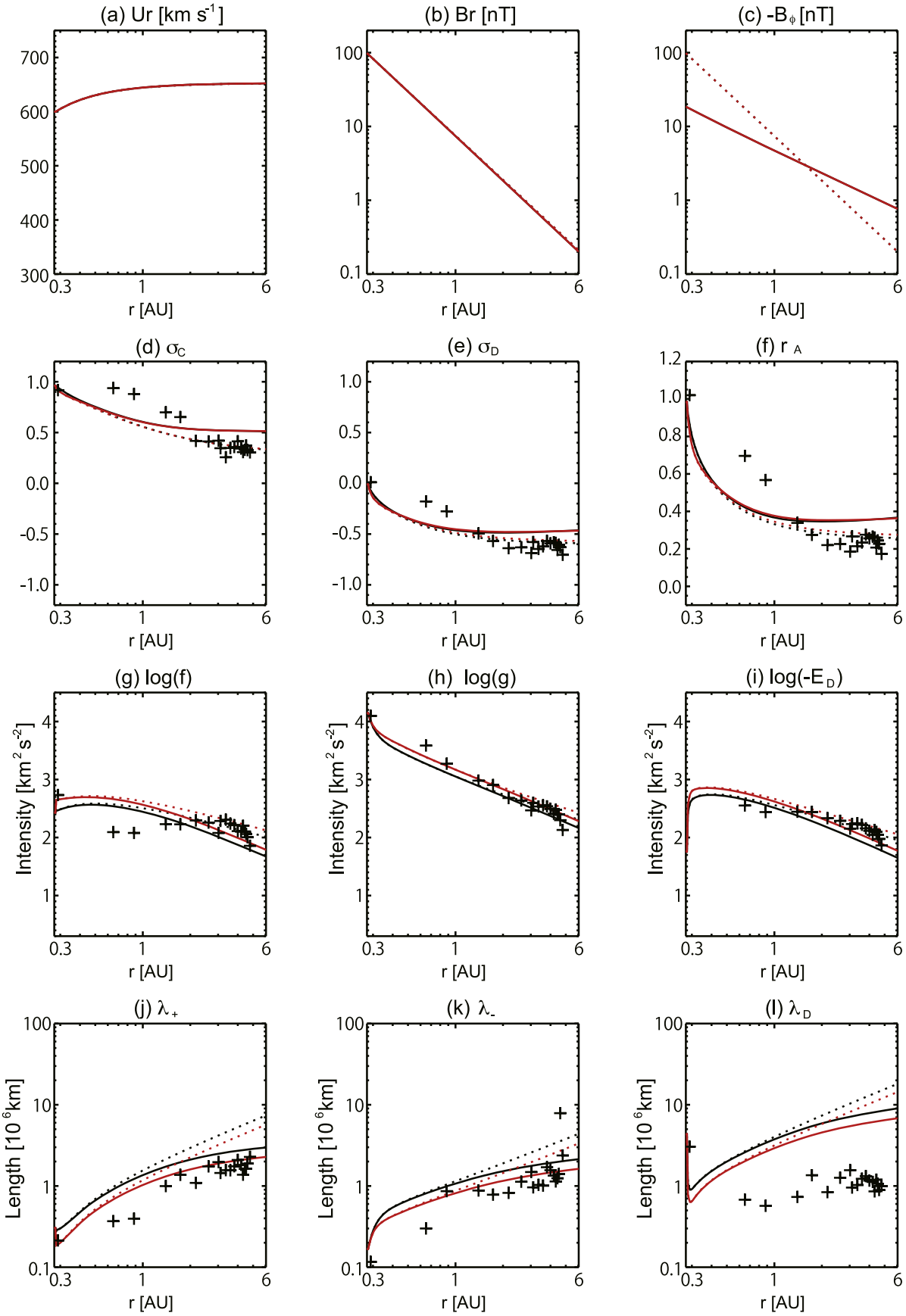

Figure 6. Comparison between Case 1 (black) and Case 4b (red). The format is the same as in Figure 3.

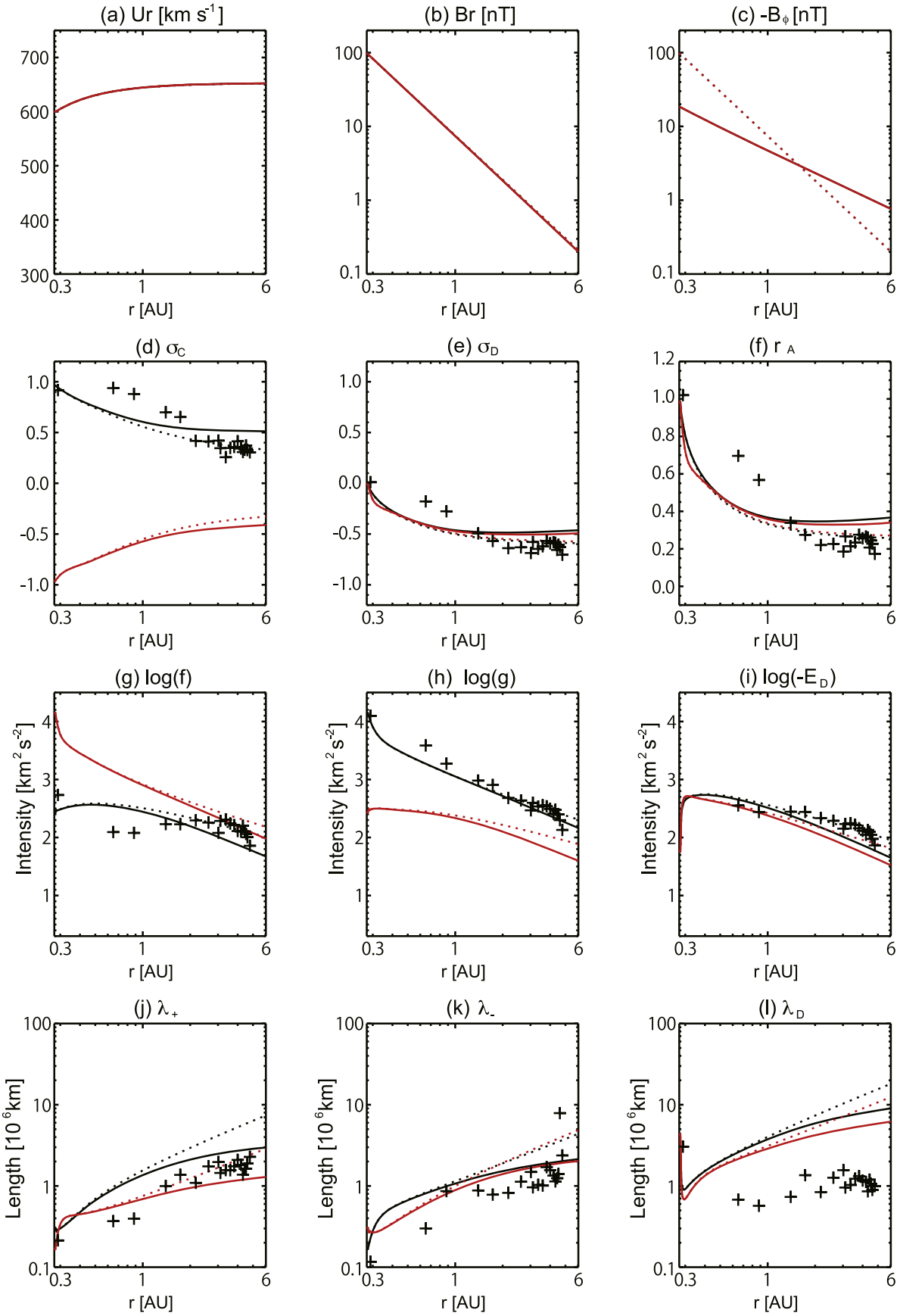

Figure 7. Comparison between Case 1 (black) and Case 5 (red). The format is the same as in Figure 3.

of the outward propagating mode g (Figure 7(h)). This indicates that the radial dependence of the turbulence intensities is strongly dependent on the values specified at the inner boundary. Around lower latitudes, the mixing between f and g is less efficient and their dissipation is stronger than at the pole.

The result shows the importance of the choice in boundary values for turbulence intensities and indicates that the highly asymmetric nature of turbulence in the fast solar wind is very likely generated in the inner heliosphere, i.e., within the inner boundary of the simulation in this study.

4. Effect of Three-dimensional Structure

In this section, we describe the effect of a non-axisymmetric solar wind and IMF on the evolution of turbulence in the inner heliosphere. First, we describe the effect of inhomogeneity of the solar wind speed (Case 6) in the next subsection, then the related effect of the IMF (Case 7a).

4.1. Effect of Inhomogeneous Solar Wind Speed

For Case 6, a tilted bimodal solar wind is introduced with the identical IMF boundary used condition in Case 1. Figures 8 and 9 show distributions of the background solar wind and turbulence variables in the meridional and equatorial planes, respectively.

In spite of the spherically symmetric radial magnetic field on the inner boundary, the magnetic field has a 3D distribution (Figures 8(b), (c), 9(b), and (c)). The radial distributions of the variables along the solid lines in Figures 8(a) and 9(a) are displayed with solid lines in each panel of Figure 10. The smallest radial flow velocity along the solid line is located around 2 au (Figure 10(a)). The magnetic field strengths of both components are enhanced behind this region and reduced ahead of it (Figures 10(b) and (c)). Before the slowest radial flow velocity, the radial gradient of the flow speed is negative, and therefore the divergence of the flow is negative, i.e., corresponding to compression (Equations (1) and (3)). Beyond the radial flow minimum, there is a positive gradient, i.e., expansion. A slight enhancement of the IMF results from the expansion and compression of the flow due to its interaction with the solar wind distribution (Figures 8(a) and 9(a)). The slightly enhanced field region ahead of fast solar wind streams is called a stream interaction region, or co-rotating interaction region (CIR) in general.

Corresponding to the IMF enhancement, the turbulence intensities of the inwardly propagating modes and the residual energy are enhanced and reduced at the same locations when considered along the equator line (the black solid lines). In contrast to the case without the flow inhomogeneity (Case 1, Figure 2), the difference in inward propagating mode intensity between on the equator (black) and 30° (blue) is within a factor of 0.1 in logarithmic scale. For Case 6, the enhancement is more than a factor of 0.2 in the equatorial plane behind the velocity minimum. In addition to the divergence and convergence effects, the solar wind speed itself affects the amplitude of the turbulence intensities as shown in Section 3.2. The slow speed effect and the expansion can explain the strong reduction in the turbulence intensities ahead of the radial flow velocity minimum (Figures 10(g) and (i)).

A consequence of the decrease in the intensities of the inward propagating mode is the rapid decrease of the cross-helicity (Figure 10(d)). In contrast, ahead of the flow speed minimum, the cross-helicity increases. The decrease ahead of the radial flow minimum can be seen in the residual energy. This results in a rapid increase in the normalized residual energy (Figure 10(e)) and Alfvén ratio (Figure 10(f)).

The various enhancements discussed above (i.e., strong inhomogeneity of the solar wind speed) can be seen mainly in the radial profiles in the equatorial plane shown in Figure 10. Because the tilt of the bipolar flow on the inner boundary is 30°, the slow wind streams located along the parallel plane are distributed in at latitudes below 30°. Spiky increases and decreases in the turbulence variables are prominent at the equator. That is interpreted as a consequence of shock formation occurring due to the nonlinear steepening of the global MHD structure.

4.2. Effect of an Inhomogeneous IMF

For Case 7a, the magnetic field boundary condition is replaced by a tilted dipole that aligns with the bipolar flow specified in Case 6. The 2D distributions in the equatorial plane are shown in Figure 11 and radial plots along a line in the equatorial plane and over both poles are shown in Figure 12. Profiles for the same locations as in Case 6 are overplotted in Figure 12 with black lines.

A comparison between Case 6 (Figure 9) and Case 7a (Figure 11) shows the effect of the inhomogeneous background IMF. Note that we specified a tilted dipole field whose strength is not spherically symmetric. The difference in the field strength can cause a slight difference in the solar wind speed profile (Figure 12(a)) compared to that of Case 6. The sign of magnetic field changes at the line perpendicular to the axis of the dipole, at which the solar wind is slowest in this model. The field strength near the magnetic neutral line is close to 0. As the solar wind propagates, the compressions and expansions described in Section 4.1 developed similarly to Case 6. However, there is no enhancement around the converging area in Case 7a. This can be understood since the compression toward the magnetic neutral line (surface) can cause the enhancement of the weak field strength region and might cause magnetic reconnection. The flow due to the reconnection can contribute to a change in the solar wind speed profiles.

Because we did not take into account the effect of the magnetic field polarity on the assumed boundary values of the turbulence, over part of the inner hemisphere (north in Case 7a and south in Case 7b, which is mentioned in the next section), the turbulence boundary values and magnetic field polarity are inconsistent. The source terms also depend on the sign of the IMF. As discussed in Section 3.5, when inappropriate turbulent intensities are specified on the boundary (Case 5) the intensity of the dominant mode decrease more rapidly than the case with appropriate boundary conditions (Case 1). Along a line on the equatorial plane in Case 7a, the polarity of the IMF is opposite before and after $r \sim 2$ au (Figure 12(b)). The IMF in the inner region ($r < 2$ au) is the same polarity as in Case 6 and that in the outer region is opposite. Comparing the turbulence intensities in the outer region in Case 6 and Case 7a shows that the influence of the boundary condition appears as a decrease in the dominant propagating mode g. In this region, g seems to be a factor of 1.3 smaller than that in Case 6. This is consistent with the results of Case 5 shown in Section 3.5. The other two intensities do not change as much. The correlation lengths in this region are shorter for the outward propagating

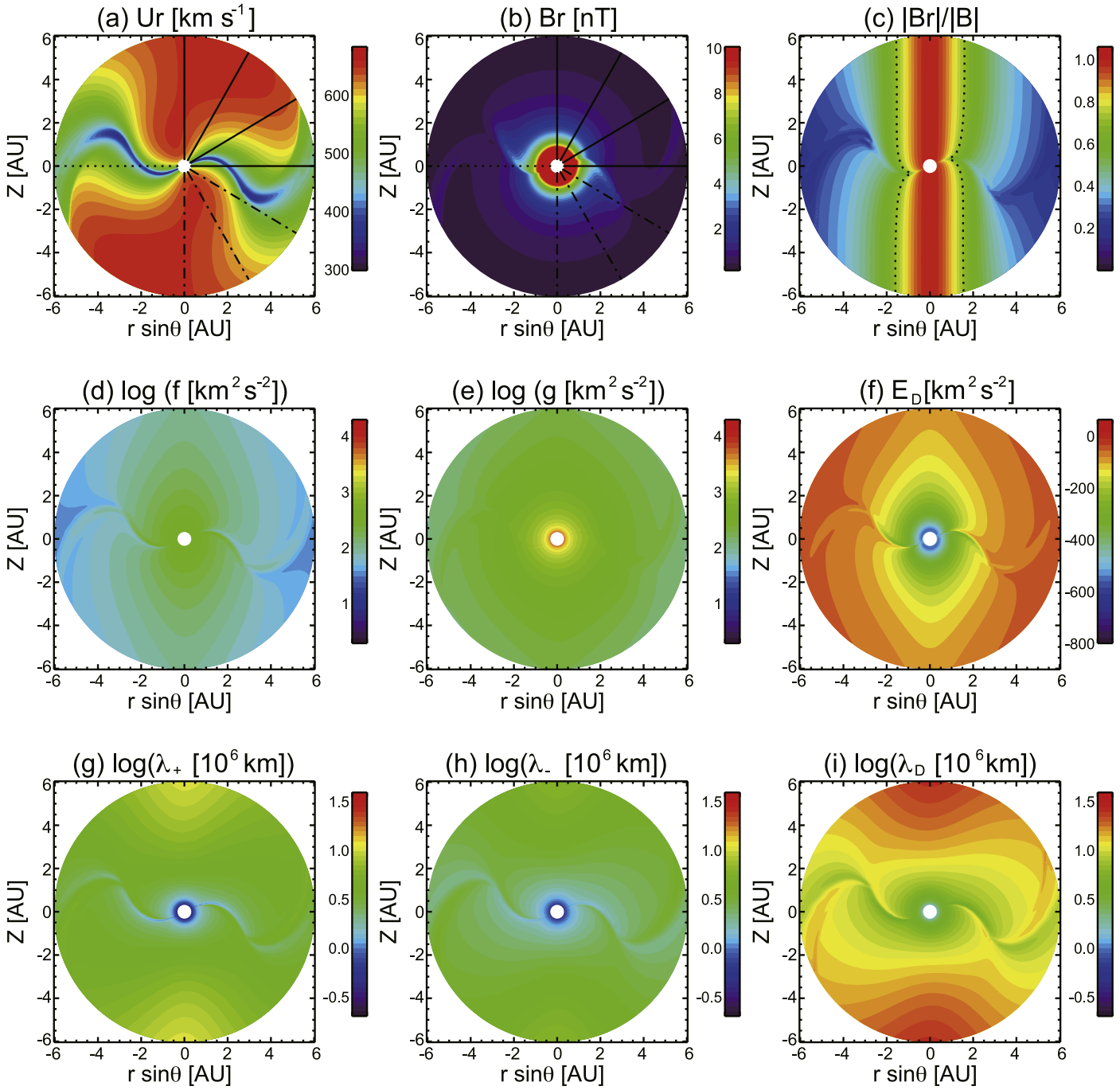

Figure 8. 2D plots in the meridional plane for Case 6. The format of each panel is the same as in Figure 1. In Panels (a) and (b), eight solid, dotted, and dotted–dashed lines display the four latitudes (0°, 30°, 60°, 90°), along which 1D profiles are drawn in Figure 10.

mode intensity f here but the other two are not different from those of Case 6.

5. Comparison with Observations

Let us now consider a fully general solar wind model with a tilted dipole magnetic field and bipolar flow (Case 7a) for the solar minimum conditions illustrated in Figures 11 and 12. The basic properties of the various turbulence moments can be understood in terms of the discussion above. However, the discussion above was based on the profiles along specific radial directions at a particular latitude and longitude. The results of our model shown above indicate a clear latitudinal distribution of the turbulence intensities. We focus here on a comparison of the model predictions with the turbulence data set used in Adhikari et al. (2015a, 2015b). As discussed above, there are certain caveats that one needs to bear in mind about combining *Helios* and *Ulysses* data, but with our 3D model, we can at least capture the 3D heliographic dependence.

Figure 13(a) shows modeled and observed profiles of the intensities of inward and outward propagating turbulent fluctuations along the orbits of *Helios* 2 (<1 au) and *Ulysses* (>1.3 au). As discussed in Section 4.2, for half of the numerical domain in Case 7a, the boundary conditions for the turbulence intensities and IMF polarities are inconsistent. We ran an auxiliary case (Case 7b) in which the turbulence boundary values and the source terms are swapped. Then the appropriate

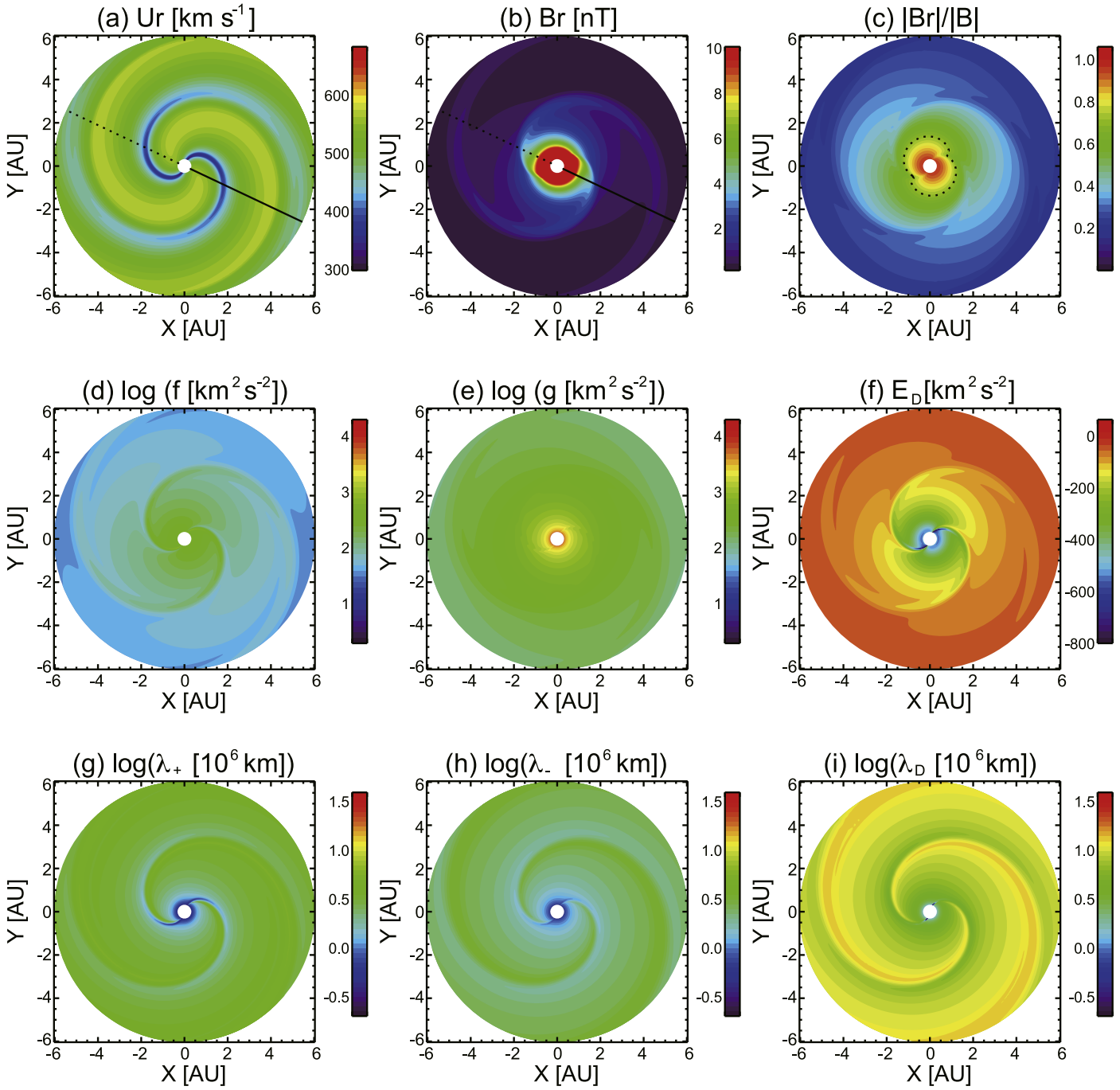

Figure 9. 2D plots on the equatorial plane for Case 6. The format of each panel is the same as in Figure 1. In Panels (a) and (b), eight solid and dotted lines display the four latitudes 0°, along which 1D profiles are drawn in Figure 10.

hemispheres in Cases 7a and 7b are combined into a complete sphere. Taking into account the actual trajectories of *Helios* and *Ulysses* in the heliosphere and the effect of the rotation of the Sun, the turbulence intensities are sampled. In the model, we specified a tilted bimodal solar wind. As a result of the rotation of the Sun, a spacecraft experiences a different longitude of the tilted wind structure every 27 days. The fluctuations in the modeled profiles in Figure 13 reflect this effect. Since the observed turbulence intensities are obtained for fast solar wind (Adhikari et al. 2015a, 2015b), the modeled profiles in the fast solar wind can account for part of the observations. The profiles of the turbulence intensities of inward and outward propagating modes are divided into two with higher background solar wind speed (>520 km s^{-1}) areas highlighted with deep colors (red and blue, respectively). The profiles of the high-speed solar winds show qualitative agreement in the radial dependence of the Elsässar intensities between 1–3 au, though the amplitudes ($r \geqslant 3$ au) are slightly smaller than those observed by *Helios* and *Ulysses*. *Helios* flew in the inner and near the ecliptic plane where slow solar wind streams exist in the model. Since the boundary conditions for the turbulence are taken for the fast solar wind in our model, the boundary conditions for turbulence in the slow solar wind may be inappropriate.

We ran an additional pair of simulations (Cases 8a and 8b) assuming the identical solar wind and IMF used in Cases 7a and 7b but now assuming that the source terms for the

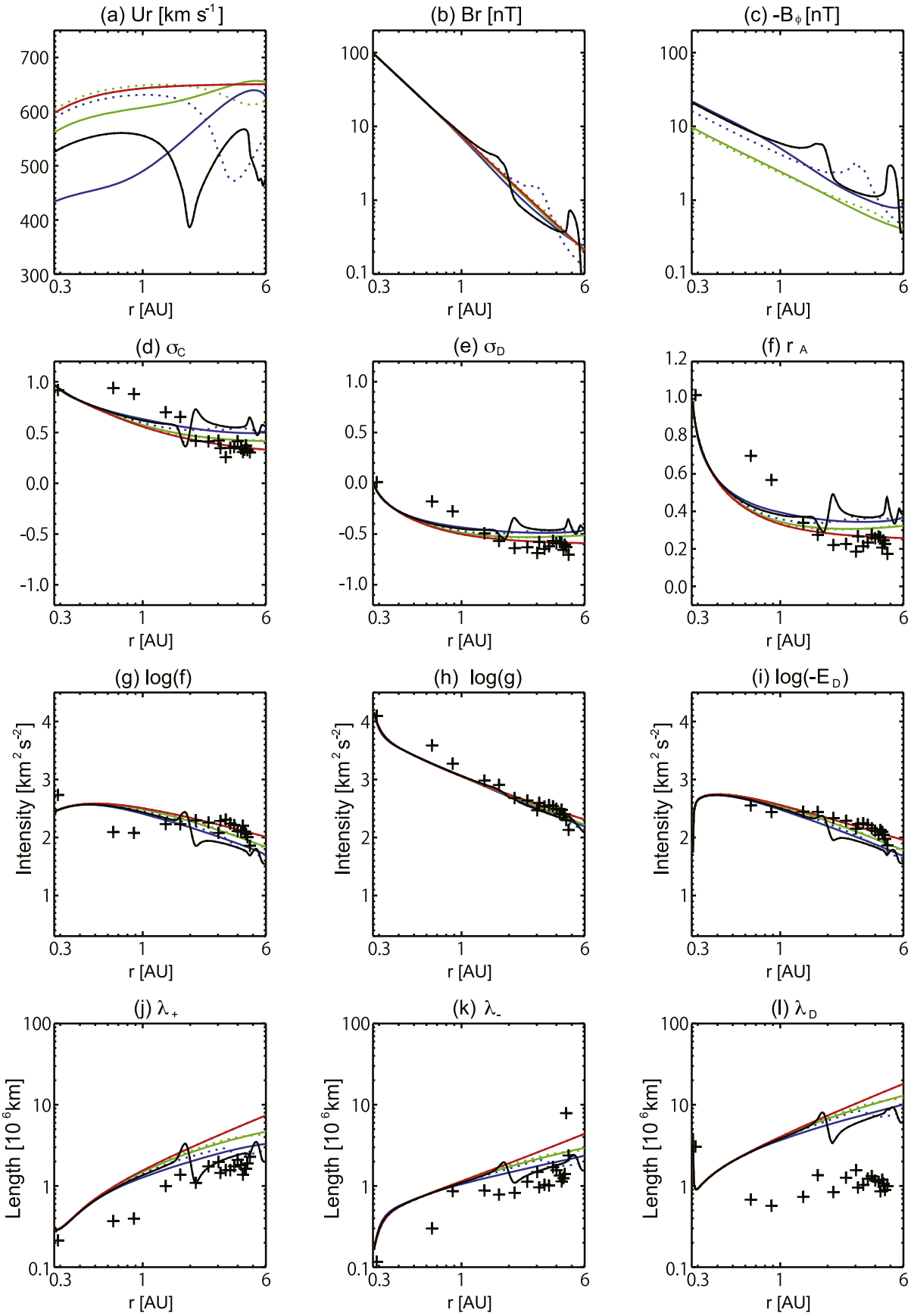

Figure 10. 1D plots along four different latitudes (0°, 30°, 60°, 90°) for Case 6. Observed values of turbulent intensities and normalized variables (Adhikari et al. 2015a) are overplotted with cross symbols in panels (d)–(i).

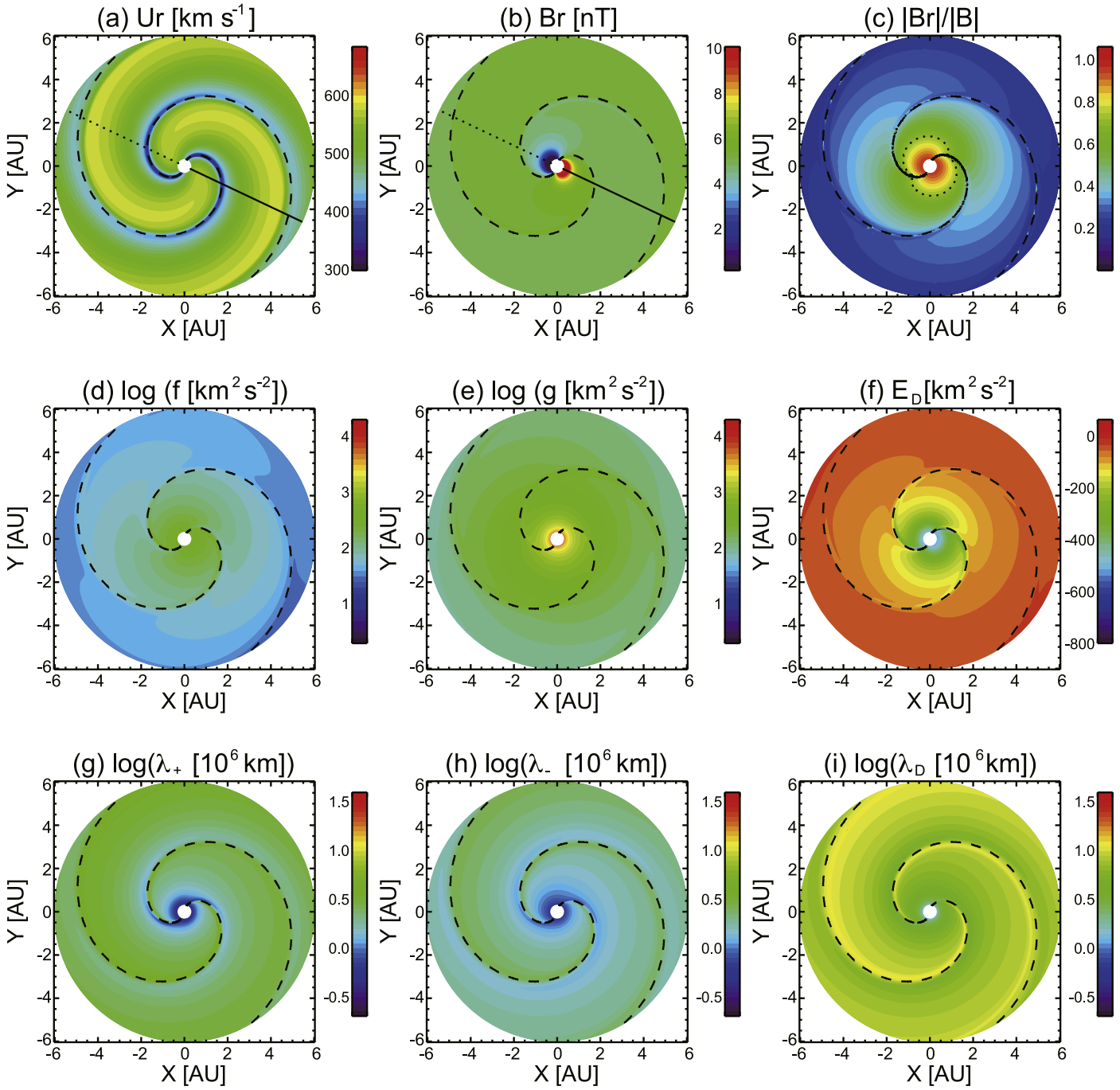

Figure 11. 2D plots in the equatorial plane for Case 7a. The format of each panel is the same as in Figure 9 except the dashed lines that indicate the polarity inversion line of IMF.

turbulence intensities are set to two times larger. As shown in Section 3.4, the twice larger source term results in a ∼1.5 factor larger amplitudes in the turbulence intensities. The results of turbulence distributions along the trajectories of *Helios* and *Ulysses* using the same method for Cases 7a and 7b are shown in Figure 13(b). The results show better quantitative agreement with the observed values.

To further understand the turbulence parameters along the trajectories of *Helios* and *Ulysses*, we collected the various modeled and observed turbulence parameters in Figure 14. It is found that the radial dependence of all parameters except for λ_D are well captured by our model. Furthermore, all the profiles except λ_D are quantitatively comparable between model and observations.

The behavior of the Alfvén ratio is closely related to the residual energy (σ_D : normalized residual energy), and the figure for σ_D shows that the kinetic and magnetic energy density in fluctuations is almost equal at 0.3 au, i.e., approximately Alfvénic. With increasing heliocentric distance, the normalized residual energy σ_D becomes increasingly negative, both in terms of the presented observations and the model, meaning that the fluctuations are dominated

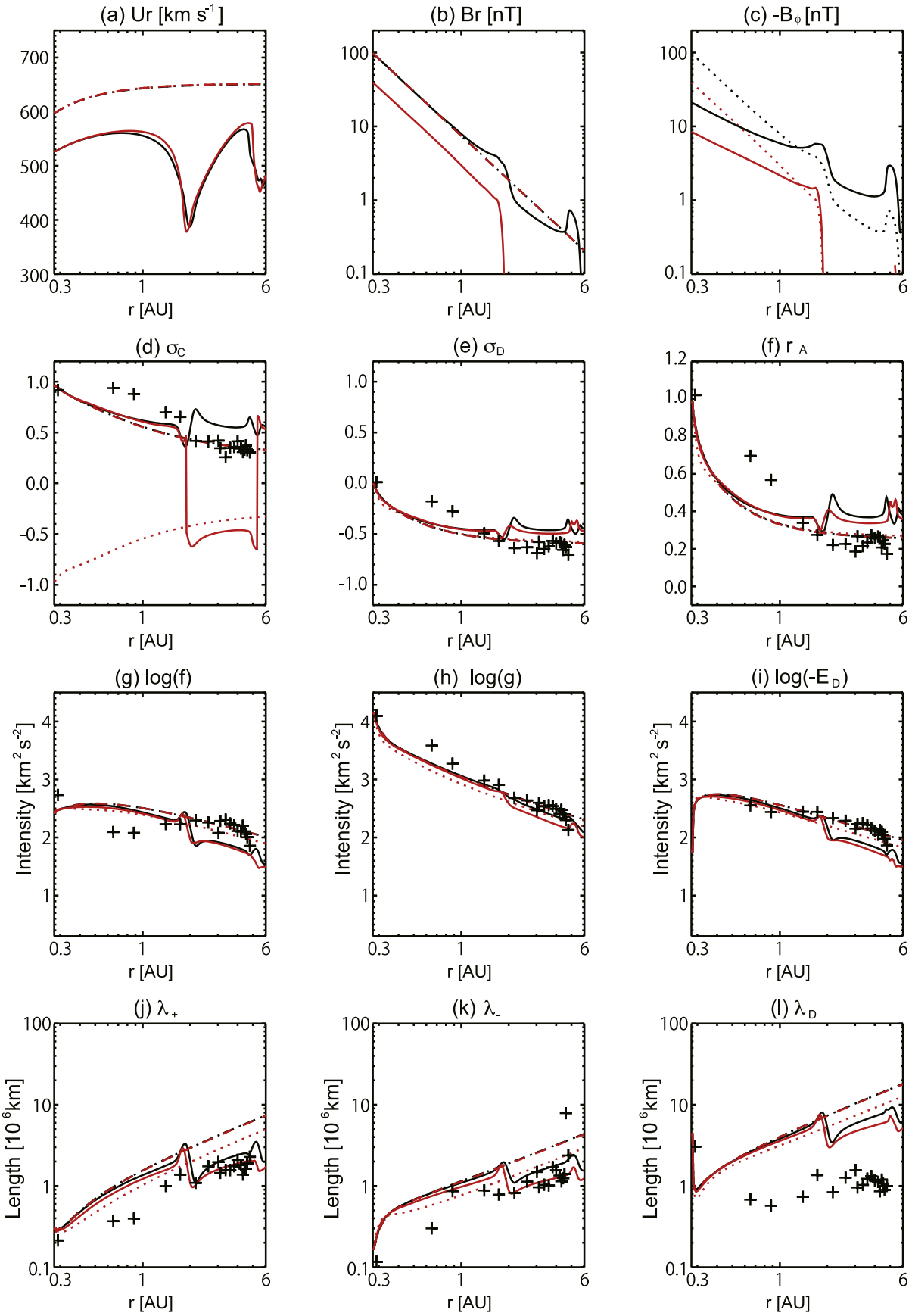

Figure 12. Comparison between Case 6 (black) and Case 7a (red). Solid line of each color in each panel displays the 1D radial plot along the equatorial line (lat = 0°), while dotted and dashed lines show that along the north and south poles (lat. = 90°) respectively.

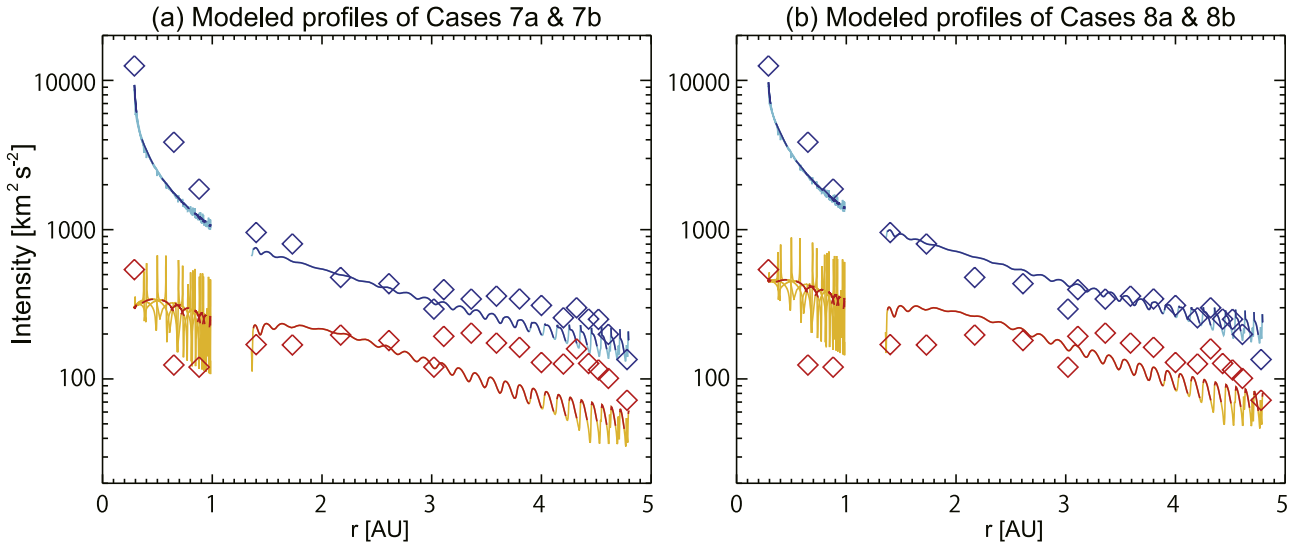

Figure 13. Modeled and observed profiles of the strength of inward and outward propagating turbulence along the orbits *Helios* 2 (<1 au) and *Ulysses* (>1.3 au). The modeled profiles where the solar wind speed exceeds 520 km s^{-1} are colored with blue (outward) and red (inward) curves while those in slower speed regions are colored with cyan (outward) and yellow (inward) curves. Observed values are displayed with diamond symbols of blue (outward) and red (inward). Panels (a) are synthesized from the results of Cases 7a and 7b, while the results in panel (b) are synthesized from the results of Cases 8a and 8b.

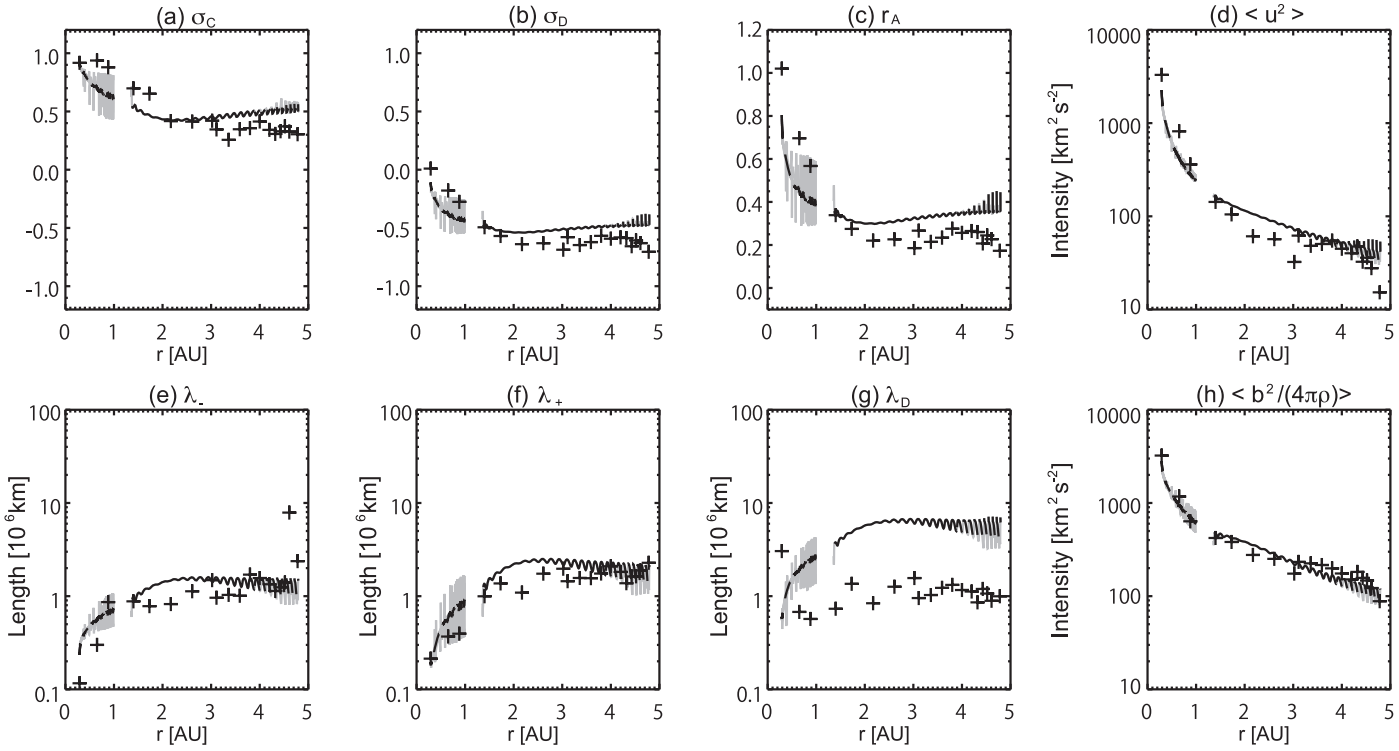

Figure 14. Modeled and observed profiles of all turbulence variables derived from the results of Cases 8a and 8b. Profiles with light gray color identify the slow solar wind while those with dark gray color correspond to fast solar wind.

increasingly by magnetic energy and not kinetic energy. In this sense, it is reasonable to suggest that the turbulence is becoming dominated by magnetic structures and is less Alfvénic. This is consistent with the conclusion of Tu & Marsch (1993).

6. Summary and Discussion

For the purpose of understanding the coupling between turbulence and solar wind, we have developed a turbulent transport model coupled with a global MHD model of solar wind on the basis of the observed photospheric magnetic field. We adopt virtually the complete form of the equations of the turbulence transport model developed by Zank et al. (2012). The unique point of this study is to take into account the effect of axisymmetric turbulence transport perpendicular to the local IMF $\boldsymbol{B}$ direction in the transport model by Zank et al. (2012), which is neglected in the previous study by Adhikari et al. (2015a). We found axisymmetric transport to be essential in

determining the latitudinal distribution of turbulence in collaboration with the global distribution of the IMF, i.e., the Parker spiral.

We performed six comparative case studies with spherically symmetric solar wind and boundary conditions to investigate the role of different background solar wind and IMF and in the sources of turbulence on the turbulence distributions. We found that all the factors considered can cause differences in the distribution characteristics of the turbulence variables. The terms of Equations (18)–(20) represent genuine source terms of turbulence driven by shear due to the presence of fast and slow streams. They are of course parametric source terms but they are not amplification terms as discussed in Section 2.3.2. The form of the residual energy arises from the definition of the residual energy based on the source terms for the inward and outward energies.

We also considered a non-axisymmetric solar wind speed distribution with a spherically symmetric IMF. Because of the interaction of solar wind flows (compression and expansion) the turbulence intensities developed complex distributions. Behind the slow solar wind, strong compression led to the formation of shocks associated with CIRs. Reflecting the compression, distributions of the inward propagating mode intensity and the residual energy exhibited spiky enhancements in these regions.

We investigated the distribution of turbulence obtained from a steady-state solar wind associated with a tilted dipole and the bipolar flow. Based on these results, synthetic profiles of the turbulence variables were calculated along the trajectories of *Helios* and *Ulysses*. The distributions are in reasonable quantitative agreement with the observed radial dependence despite our not trying to adjust boundary conditions or parameters to achieve an accurate fit.

The cross-coupling between MHD and turbulence, validated with observations in present and future missions such as Solar Orbiter and Solar Probe Plus, is expected to improve the model and yield greater understanding of turbulence in the solar wind. The parameters would be improved by the validation with present and future observations.

In this study, we adopt only the effects of global solar wind inhomogeneity on the turbulence transport. However, in the actual solar wind, the heating of the solar wind caused by its interaction with turbulence is expected to play an important role in the dynamics of the solar corona and solar wind. A more advanced model considering cross-coupling in both directions between MHD and turbulence is expected to reproduce a more realistic distribution of solar wind and turbulence.

One of the key factors in our modeling is the boundary values of the turbulence variables. In this paper, we did not study the appropriate boundary values. It is known that properties of turbulence are very different between fast and slow solar winds (Bruno & Carbone 2005, 2013). In fast solar wind, the turbulence has anisotropic (the cross-helicity $\sigma_C \sim 1$) and highly Alfvénic (the residual energy $\sigma_D \sim 0$) properties, while $\sigma_C \sim 0$ and $\sigma_D \sim -1$ in the slow wind. The boundary values used in the current study are those for the fast solar wind. Hence the turbulence intensities in slow solar wind regions are not well modeled. Further studies are needed to specify the appropriate values.

This work was supported by JSPS KAKENHI Grant Number 26800255 and 26106006. This work was carried out as a computational joint research program at the Institute for Space and Earth Environmental Research, Nagoya University. G.P.Z., P.H., and L.A. acknowledge the support of a Solar Probe Plus subcontract through the Harvard-Smithsonian Center for Astrophysics SV4-84017 and a NASA grant NNX14AC08G. D.T. is financially supported by the Italian Space Agency (ASI) under contract I/013/12/0. Data from *Helios* and *Ulysses* were obtained from the NASA CDAWeb website.

Appendix A
Derivation of the Turbulent Transport Equations

The transport equations describing low-frequency MHD turbulence in a large-scale inhomogeneous flow are derived by taking moments of Equation (7) (Zank et al. 2012), corresponding to Equations (42), (43), (44), (27), and (29) of Zank et al. (2012):

$$\frac{\partial f}{\partial t} = -(\boldsymbol{U}-\boldsymbol{V}_A)\cdot\nabla f - \nabla\cdot\left(\frac{\boldsymbol{U}}{2}+\boldsymbol{V}_A\right)(f-E_D) - 2\frac{f^2\sqrt{g}}{L^+} + 2S^+ - 2\left[\nabla\cdot(a\boldsymbol{U}+b\boldsymbol{V}_A) + \frac{b\boldsymbol{V}_A\cdot\nabla\rho}{2\rho} - n_i n_j\left(\frac{\partial}{\partial x_i}(aU_j+bV_{Aj}) + \frac{bV_{Aj}}{2\rho}\frac{\partial\rho}{\partial x_i}\right)\right]E_D; \quad (25)$$

$$\frac{\partial g}{\partial t} = -(\boldsymbol{U}+\boldsymbol{V}_A)\cdot\nabla g - \nabla\cdot\left(\frac{\boldsymbol{U}}{2}-\boldsymbol{V}_A\right)(g-E_D) - 2\frac{g^2\sqrt{f}}{L^-} + 2S^- - 2\left[\nabla\cdot(a\boldsymbol{U}-b\boldsymbol{V}_A) - \frac{b\boldsymbol{V}_A\cdot\nabla\rho}{2\rho} - n_i n_j\left(\frac{\partial}{\partial x_i}(aU_j-bV_{Aj}) - \frac{bV_{Aj}}{2\rho}\frac{\partial\rho}{\partial x_i}\right)\right]E_D; \quad (26)$$

$$\begin{aligned}\frac{\partial E_D}{\partial t} = &-\boldsymbol{U}\cdot\nabla E_D - \frac{\nabla\cdot\boldsymbol{U}}{2}\left(E_D-\frac{f+g}{2}\right) - \nabla\cdot\boldsymbol{V}_A\frac{f-g}{2} - \left[\nabla\cdot(a\boldsymbol{U}-b\boldsymbol{V}_A) - \frac{b\boldsymbol{V}_A\cdot\nabla\rho}{2\rho} - n_i n_j\left(\frac{\partial}{\partial x_i}(aU_j-bV_{Aj}) - \frac{bV_{Aj}}{2\rho}\frac{\partial\rho}{\partial x_i}\right)\right]f \\ &- \left[\nabla\cdot(a\boldsymbol{U}+b\boldsymbol{V}_A) + \frac{b\boldsymbol{V}_A\cdot\nabla\rho}{2\rho} - n_i n_j\left(\frac{\partial}{\partial x_i}(aU_j+bV_{Aj}) + \frac{bV_{Aj}}{2\rho}\frac{\partial\rho}{\partial x_i}\right)\right]g \\ &- \frac{1}{2}\left(\sqrt{\frac{f}{g}}\boldsymbol{V}_A\cdot\nabla g - \sqrt{\frac{g}{f}}\boldsymbol{V}_A\cdot\nabla f\right) - \left[\frac{g\sqrt{f}}{L^-} - \frac{f\sqrt{g}}{L^+}\right]E_D + 2S_D, \end{aligned} \quad (27)$$

$$\frac{\partial L^{\pm}}{\partial t} = -(\boldsymbol{U} \mp \boldsymbol{V}_A)\cdot\nabla L^{\pm} - \nabla\cdot\left(\frac{\boldsymbol{U}}{2} \pm \boldsymbol{V}_A\right)\left(L^{\pm} - \frac{L^D}{2}\right) - \left[\nabla\cdot(a\boldsymbol{U} \pm b\boldsymbol{V}_A) \pm \frac{b\boldsymbol{V}_A\cdot\nabla\rho}{2\rho} - n_i n_j\left(\frac{\partial}{\partial x_i}(aU_j \pm bV_{Aj}) \pm \frac{bV_{Aj}}{2\rho}\frac{\partial\rho}{\partial x_i}\right)\right]L_D \quad (28)$$

$$\frac{\partial L^D}{\partial t} = -\boldsymbol{U}\cdot\nabla L^D - \frac{\nabla\cdot\boldsymbol{U}}{2}(L^D - L^+ - L^-) - \left(\sqrt{\frac{L^+}{L^-}}\boldsymbol{V}_A\cdot\nabla L^- - \sqrt{\frac{L^-}{L^+}}\boldsymbol{V}_A\cdot\nabla L^+\right) - \nabla\cdot\boldsymbol{V}_A(L^+ - L^-) - 2\left[\nabla\cdot(a\boldsymbol{U} - b\boldsymbol{V}_A) - \frac{b\boldsymbol{V}_A\cdot\nabla\rho}{2\rho} - n_i n_j\left(\frac{\partial}{\partial x_i}(aU_j - bV_{Aj}) - \frac{bV_{Aj}}{2\rho}\frac{\partial\rho}{\partial x_i}\right)\right]L^+ - 2\left[\nabla\cdot(a\boldsymbol{U} + b\boldsymbol{V}_A) + \frac{b\boldsymbol{V}_A\cdot\nabla\rho}{2\rho} - n_i n_j\left(\frac{\partial}{\partial x_i}(aU_j + bV_{Aj}) + \frac{bV_{Aj}}{2\rho}\frac{\partial\rho}{\partial x_i}\right)\right]L^- \quad (29)$$

where $\boldsymbol{n}$ is the axisymmetric direction of turbulence. With the assumption $\boldsymbol{n} = \boldsymbol{B}/B$, Equations (25) to (29) are reduced as follows:

$$\frac{\partial f}{\partial t} = -(\boldsymbol{U} - \boldsymbol{V}_A)\cdot\nabla f - \nabla\cdot\left(\frac{\boldsymbol{U}}{2} + \boldsymbol{V}_A\right)f + \left[\nabla\cdot\left(\frac{\boldsymbol{U}}{2} + \boldsymbol{V}_A\right) - 2(M_1 + M_2)\right]\times E_D - 2\frac{f^2\sqrt{g}}{L^+} + 2S^+ \quad (30)$$

$$\frac{\partial g}{\partial t} = -(\boldsymbol{U} + \boldsymbol{V}_A)\cdot\nabla g - \nabla\cdot\left(\frac{\boldsymbol{U}}{2} - \boldsymbol{V}_A\right)g + \left[\nabla\cdot\left(\frac{\boldsymbol{U}}{2} - \boldsymbol{V}_A\right) - 2(M_1 - M_2)\right]\times E_D - 2\frac{g^2\sqrt{f}}{L^-} + 2S^- \quad (31)$$

$$\frac{\partial E_D}{\partial t} = -\boldsymbol{U}\cdot\nabla E_D + \left[\nabla\cdot\left(\frac{\boldsymbol{U}}{2} - \boldsymbol{V}_A\right) - 2(M_1 - M_2)\right]\frac{f}{2} + \left[\nabla\cdot\left(\frac{\boldsymbol{U}}{2} + \boldsymbol{V}_A\right) - 2(M_1 + M_2)\right]\frac{g}{2} - \frac{\nabla\cdot\boldsymbol{U}}{2}E_D - \frac{1}{2}\left(\sqrt{\frac{f}{g}}\boldsymbol{V}_A\cdot\nabla g - \sqrt{\frac{g}{f}}\boldsymbol{V}_A\cdot\nabla f\right) - \left[\frac{g\sqrt{f}}{L^-} - \frac{f\sqrt{g}}{L^+}\right]E_D + 2S_D \quad (32)$$

$$\frac{\partial L^{\pm}}{\partial t} = -(\boldsymbol{U} \mp \boldsymbol{V}_A)\cdot\nabla L^{\pm} - \nabla\cdot\left(\frac{\boldsymbol{U}}{2} \pm \boldsymbol{V}_A\right)L^{\pm} + \left[\frac{1}{2}\nabla\cdot\left(\frac{\boldsymbol{U}}{2} \pm \boldsymbol{V}_A\right) - (M_1 \pm M_2)\right]L_D \quad (33)$$

$$\frac{\partial L^D}{\partial t} = -\boldsymbol{U}\cdot\nabla L^D - \frac{\nabla\cdot\boldsymbol{U}}{2}L^D - \left(\sqrt{\frac{L^+}{L^-}}\boldsymbol{V}_A\cdot\nabla L^- - \sqrt{\frac{L^-}{L^+}}\boldsymbol{V}_A\cdot\nabla L^+\right) + \left[\frac{\nabla\cdot\boldsymbol{U}}{2} - \nabla\cdot\boldsymbol{V}_A - 2(M_1 - M_2)\right]L^+ + \left[\frac{\nabla\cdot\boldsymbol{U}}{2} + \nabla\cdot\boldsymbol{V}_A - 2(M_1 + M_2)\right]L^- \quad (34)$$

where

$$\begin{aligned} M_1 &= a\left[\nabla\cdot\boldsymbol{U} - \frac{(\boldsymbol{B}\cdot\nabla\boldsymbol{U})}{B^2}\cdot\boldsymbol{B}\right] \\ &= a\left[\nabla\cdot\boldsymbol{U} - \frac{B_r^2}{B^2}\frac{\partial U_r}{\partial r} - \frac{B_\theta^2}{B^2}\left(\frac{1}{r}\frac{\partial U_\theta}{\partial\theta} + \frac{U_r}{r}\right) - \frac{B_\phi^2}{B^2}\left(\frac{1}{r\sin\theta}\frac{\partial U_\phi}{\partial\phi} + \frac{U_r}{r} + \frac{U_\theta\cot\theta}{r}\right) - \frac{B_r B_\theta}{B^2}\left(\frac{1}{r}\frac{\partial U_r}{\partial\theta} + \frac{\partial U_\theta}{\partial r} - \frac{U_\theta}{r}\right) - \frac{B_\theta B_\phi}{B^2}\left(\frac{1}{r\sin\theta}\frac{\partial U_\theta}{\partial\phi} + \frac{1}{r}\frac{\partial U_\phi}{\partial\theta} - \frac{U_\phi\cot\theta}{r}\right) - \frac{B_\phi B_r}{B^2}\left(\frac{1}{r}\frac{\partial U_\phi}{\partial r} + \frac{1}{r\sin\theta}\frac{\partial U_r}{\partial\phi} - \frac{U_\phi}{r}\right)\right] \\ &\quad - \sim a\left[\nabla\cdot\boldsymbol{U} - \frac{B_r^2}{B^2}\frac{\partial U_r}{\partial r} - \frac{B_\theta^2 + B_\phi^2}{B^2}\frac{U_r}{r}\right] \end{aligned} \quad (35)$$

$$\begin{aligned} M_2 &= b\left[\nabla\cdot\boldsymbol{V}_A - \frac{(\boldsymbol{B}\cdot\nabla\boldsymbol{V}_A)}{B^2}\cdot\boldsymbol{B} + \frac{\boldsymbol{V}_A\cdot\nabla\rho}{2\rho} - \frac{B_i B_j}{B^2}\frac{V_{Aj}}{2\rho}\frac{\partial\rho}{\partial x_i}\right] \\ &= b\left[\nabla\cdot\boldsymbol{V}_A - \frac{B_r^2}{B^2}\frac{\partial V_{Ar}}{\partial r} - \frac{B_\theta^2}{B^2}\frac{1}{r}\frac{\partial V_{A\theta}}{\partial\theta} - \frac{B_\phi^2}{B^2}\frac{1}{r\sin\theta}\frac{\partial V_{A\phi}}{\partial\phi} - \frac{B_r B_\theta}{B^2}\left(\frac{1}{r}\frac{\partial V_{Ar}}{\partial\theta} + \frac{\partial V_{A\theta}}{\partial r}\right) - \frac{B_\theta B_\phi}{B^2}\left(\frac{1}{r\sin\theta}\frac{\partial V_{A\theta}}{\partial\phi} + \frac{1}{r}\frac{\partial V_{A\phi}}{\partial\theta}\right) - \frac{B_\phi B_r}{B^2}\left(\frac{1}{r}\frac{\partial V_{A\phi}}{\partial r} + \frac{1}{r\sin\theta}\frac{\partial V_{Ar}}{\partial\phi}\right)\right] \\ &= b\left[\nabla\cdot\boldsymbol{V}_A - \frac{\boldsymbol{B}\cdot\nabla(V_A^2)}{2\,|V_A||B|}\right] \\ &= b\left[\nabla\cdot\boldsymbol{V}_A - \frac{\boldsymbol{B}\cdot\nabla\,|V_A|}{|B|}\right] \end{aligned} \quad (36)$$

are mixing terms. In the final line of Equation (35), we obtain a simple form by assuming the approximation $\boldsymbol{U} = U_r \boldsymbol{e}_r$. The third and fourth terms of the right side of Equation (36) (including ρ) must vanish because they are identical. As described in Zank et al. (2012), we are free to choose the parameters a and b. We chose $a = 1/2$ and $b = 1/2$ invoking two-dimensional turbulence perpendicular to the global magnetic field.

Appendix B
The Auto-Correlation Function and the Correlation Length

In comparing our theoretical model against observations, we used the results derived by Adhikari et al. (2015a) from *Helios* 2 data for the inner boundary conditions at 0.3 au and as observations at different distances against which to compare the theoretical model. Specifically, this included a derivation of the auto-correlation functions and the various correlation lengths from the plasma and magnetometer data sets obtained by *Helios* 2. In the main text, we showed the observed correlation lengths corresponding to forward and backward propagating modes, and the residual energy at distances of 0.87, 0.65, and 0.29 au. A study of the correlation length λ_- estimated from the observed auto-correlation function at 0.29 au and 0.87 au was presented by Marsch & Tu (1990; their Figure 1), where they obtained a value that is larger by an order of magnitude than the one used here. We show here that the analysis of Marsch & Tu (1990) over-estimates the correlation length and that the correct value is that given in Adhikari et al. (2015a). As discussed below, the primary difference between the two studies resides in the fact that, unlike Marsch & Tu (1990), we properly take into account the non-stationarity of the solar wind.

At the distances of 0.29 au and 0.87 au, *Helios* 2 sampled a high-speed stream coming from the same source region at the Sun during three consecutive solar rotations (Bruno 1992). Here, we consider the derivation of the auto-correlation functions and the related correlation lengths of forward and backward propagating modes. To derive the correlation length, we first calculate the auto-correlation function of a time series data set as a function of lag L. The lag L is the separation distance between two-point measurements, i.e., $\langle z^+(x) z^+(x+L)\rangle$, where we assume Taylor's frozen-in condition to translate time and velocity to a spatial lag L. To estimate the correlation length, we integrate the two-point auto-correlation function over L, i.e., $\int_0^\infty \langle z^+(x) z^+(x+L)\rangle dL = \lambda_+ \langle z^{+2}\rangle$, where $\langle z^{+2}\rangle$ is the auto-correlation evaluated at $L = 0$. It is sufficiently accurate to integrate up to $1/e$ of the maximum value of the auto-correlation function at zero lag. Recall that the use of $1/e$ is in fact consistent with the derivation of the auto-correlation function (see Bruno & Carbone 2013) or from the assumption that turbulent decay is inversely proportional to the correlation length. It is extremely important to note that the lengths of the interval of the data sets have to be chosen carefully when seeking correlations in solar wind fluctuations. The reason for the importance is because, as one increases the interval length, it is possible that one can (inadvertently) include the structure of streams, for example, which then results in an increased auto-correlation function and correlation length. Consequently, a longer interval data set may not necessarily be of help in determining correlations within the inertial range in solar wind turbulence.

To account for the possibility that the solar wind is not stationary, we considered a statistical set of 12 hr intervals within a period of two days for all three heliocentric distances. We assumed that 12 hours of data is sufficient to determine the correlations existing between the turbulent fluctuations in the inertial range. In performing the analysis over a 12 hr window, we moved in steps of 81 seconds (the *Helios* 2 sampling time) along the stream for two days, from day of year (DOY) 105.5 to 107.5. Since there are 2133 data points within a two day set of data with an 81 s sampling time and a window of 12 hours corresponds to 533 data points, the analysis was therefore performed for 1600 different time intervals of 12 hours each within a period of two days. From the plasma and magnetometer data sets of the *Helios* 2 spacecraft, we first calculated the Elsässer variables $z^\pm$. The analysis yields 1600 auto-correlation functions corresponding to z^- and the same number of correlation lengths λ_-. The left plot of Figure 15 shows the auto-correlation functions of z^- and the right plot the auto-correlation functions of z^+, both at 0.3 au. The average of these functions, as well as the corresponding correlation lengths, can be considered a reasonable estimate of the turbulence characteristics of the non-stationary solar wind. The left plot of Figure 15 shows black curves that correspond to the 1600 auto-correlation functions of z^-, the red curve is the average of the black curves, and the green curve the auto-correlation function computed in the two day period as a whole. The auto-correlation functions are correctly normalized to the zero-lag value. The first point shown is at a lag of 81 seconds, where the auto-correlation function is very close to one. The large variability of the auto-correlation functions in Figure 15 is due to the solar wind not being stationary. The averaged estimate of the auto-correlation function is statistically more correct than that obtained by considering the two day data set as a whole. Indeed, computing the auto-correlation function in the whole two day interval means that the non-stationarity of the solar wind has not been accounted for, thus leading to less reliable correlation lengths. It is clear from the much larger value for the whole two day period that the temporal solar wind has to be accounted for in a statistical analysis of the auto-correlation function. Unlike Marsch & Tu (1990), where the auto-correlation functions were computed over the entire data sets, the approach described here properly captures the non-stationarity of the solar wind in the analysis.

Figure 15 illustrates the important result that the auto-correlation function corresponding to the full two day interval (green curve) is larger than that corresponding to an average derived from auto-correlations obtained using 12 hr intervals (red curve) spanning the two day period. In Figure 15, the horizontal dashed line identifies $1/e$ of the value of the auto-correlation function at zero lag. From Figure 15, we can estimate the correlation length directly from its definition. From the left plot of Figure 15, the correlation lengths λ_- corresponding to the red and green curves can be estimated as 0.11×10^6 km and 1.8×10^6 km, respectively. Similarly, the right plot of Figure 15 yields correlation lengths λ_+ corresponding to the red and green curves as approximately 0.22×10^6 km and 0.32×10^6 km, respectively. Quite interestingly, despite Marsch & Tu (1990) using a different definition of the correlation length, they found correlation lengths fairly close to those obtained here when considering auto-correlation functions computed over the whole data set (green curves in Figure 15), i.e., when the non-stationarity of

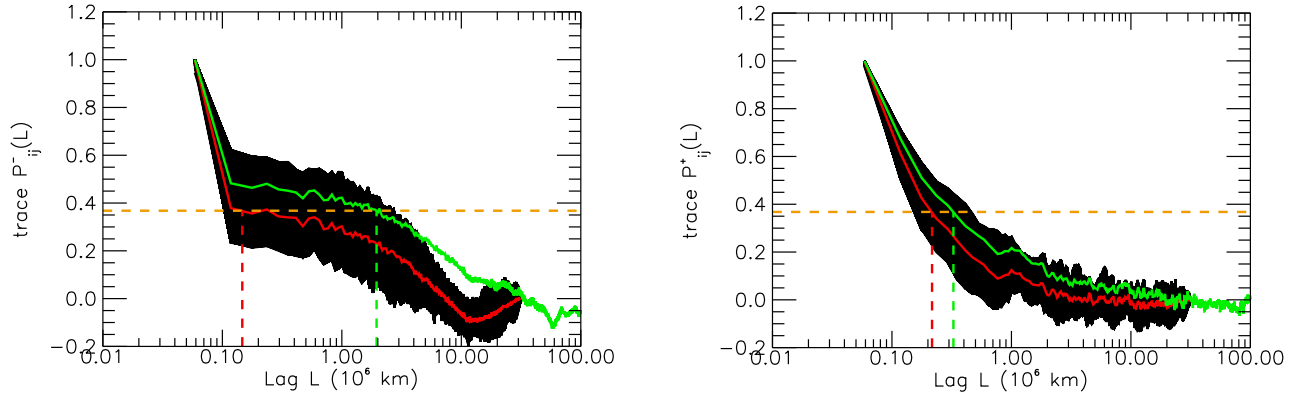

Figure 15. Left: auto-correlation functions of z^- at 0.3 au as a function of lag L. Right: auto-correlation functions of z^+ at 0.3 au as a function of lag L. The black curves show auto-correlation functions for each 12 hr interval data set within a two day period. The red curves show the average of the auto-correlation functions. The green curve shows the auto-correlation function for a full two day period. The horizontal dashed curves identify 0.36 of the maximum value of the auto-correlation function at zero lag.

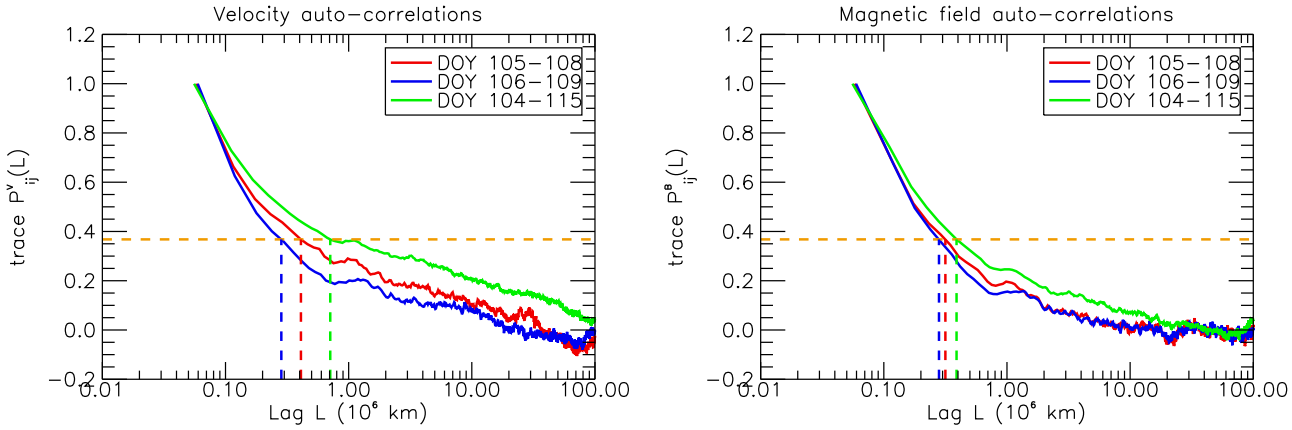

Figure 16. Left: the normalized auto-correlation function of the velocity at 0.3 au as a function of lag L. Right: the normalized auto-correlation function of the magnetic field at 0.3 au as a function of time lag. The red curves show the normalized auto-correlation function for DOY 105–108, the blue curves for DOY 106–109, and the green curves for DOY 104–115.

the solar wind is not properly taken into account in the analysis. Indeed, Marsch & Tu (1990) derived the auto-correlation functions using the entire three day period despite the presence of time-dependent stream structure and the non-stationarity of the solar wind plasma. This is an explicit demonstration of the importance of accounting for non-stationarity in the analysis of turbulent fluctuations in the solar wind.

The fact that the auto-correlation function of z^- increases when the time interval is longer (green curve of Figure 15) suggests that the outflow speed of the solar wind plays an important role in determining the z^- auto-correlation function. This is confirmed by the left and right plots of Figure 16, which show that the auto-correlation function of the velocity (left plot of Figure 16) especially increases with a longer time interval (green curve). Conversely, the magnetic field is less dependent on the duration of the interval (right plot of Figure 16). In Figure 16, the solid blue curves illustrate the normalized auto-correlation function for DOY 106–109, the green curves for DOY 104–115, and the red curves for DOY 105–108. From the left plot of Figure 16, the correlation lengths corresponding to the velocity fluctuations for DOY 105–108, 106–109, and 104–115 can be estimated approximately as 0.42×10^6 km, 0.28×10^6 km, and 0.72×10^6 km, respectively. Similarly, the correlation lengths corresponding to the magnetic field fluctuations for DOY 105–108, 106–109, and 104–115 can be estimated approximately as 0.32×10^6 km, 0.28×10^6 km, and 0.38×10^6 km, respectively.

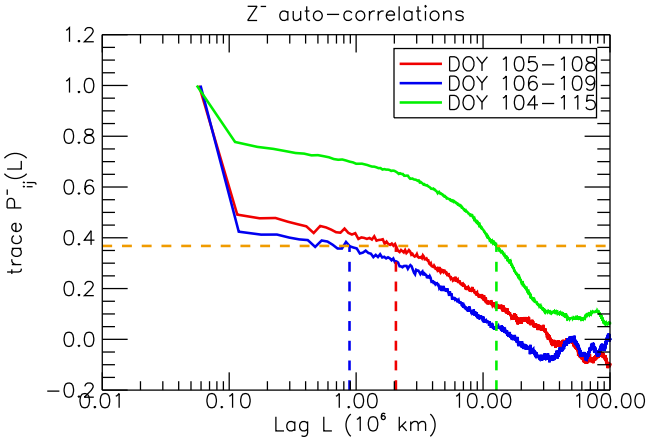

Figure 17. Normalized auto-correlation function z^- at 0.3 au using different intervals as a function of lag L. The red curve shows the normalized auto-correlation function for the interval DOY 105–108, the blue curve for DOY 106–109, and the green curve for DOY 104–115.

To complete our analysis, we investigated the dependence of the auto-correlation function of z^- on the location of the time interval of the data set. Figure 17 shows that the z^- auto-correlation function depends not only on the length of the

time interval, but also on where the time interval is taken within the same stream. In Figure 17, the red and blue curves both refer to a four day period, with the red curve corresponding to the interval DOY 105–108, and the blue curve to the interval DOY 106–109. The green curve shows the auto-correlation function of z^- for the full interval DOY 104–115. Figure 17 shows that there is a significant difference between the two auto-correlation functions, due to the solar wind not being stationary. On using Figure 17, the correlation lengths of z^- can be estimated for the intervals DOY 105–108, 106–109, and 104–115 as approximately 2.2×10^6 km, 0.19×10^6 km, and 10.2×10^6 km, respectively. These correlation lengths are derived from the auto-correlation functions, which are maximum at zero lag.

References

Adhikari, L., Zank, G. P., Bruno, R., et al. 2015a, ApJ, 805, 63
Adhikari, L., Zank, G. P., Bruno, R., et al. 2015b, JPhCS, 642, 012001
Adhikari, L., Zank, G. P., Hu, Q., & Dosch, A. 2014, ApJ, 793, 52
Arge, C. N., & Pizzo, V. J. 2000, JGR, 105, 10465
Belcher, J. W., & Davis, L., Jr. 1971, JGR, 76, 3534
Breech, B., Matthaeus, W. H., Minnie, J., et al. 2008, JGRA, 113, 8105
Bruno, R., & Carbone, V. 2005, LRSP, 2, 4
Bruno, R., & Carbone, V. 2013, LRSP, 10, 2
Bruno, R., D'Amicis, R., Bavassano, B., Carbone, V., & Sorriso-Valvo, L. 2007, AnGeo, 25, 1913
Bruno, R. 1992, in Solar Wind Seven (Proc. of the 3rd COSPAR Colloquium), ed. E. Marsch & R. Schwenn (Oxford: Pergamon Press)
Coleman, P. J., Jr. 1968, ApJ, 153, 371
Dedner, A., Kemm, F., Kröner, D., et al. 2002, JCoPh, 175, 645
Elsässer, W. M. 1950, PhRv, 79, 183
Hayashi, K., Kojima, M., Tokumaru, M., & Fujiki, K. 2003, JGRA, 108, 1102
Hunana, P., & Zank, G. P. 2010, ApJ, 718, 148
Kageyama, A., & Sato, T. 2004, GGG, 5, 9005
Kryukov, I. A., Pogorelov, N. V., Zank, G. P., & Borovikov, S. N. 2012, in AIP Conf. Ser. 1436, Physics of the Heliosphere: A 10 Year Retrospective, ed. J. Heerikhuisen et al. (Melville, NY: AIP), 48
Lee, M. A., & Ip, W.-H. 1987, JGR, 92, 11041
Marsch, E., & Tu, C.-Y. 1989, JPlPh, 41, 479
Marsch, E., & Tu, C.-Y. 1990, JGR, 95, 8211
Matthaeus, W. H., Zank, G. P., Oughton, S., Mullan, D. J., & Dmitruk, P. 1999a, ApJL, 523, L93
Matthaeus, W. H., Zank, G. P., Smith, C. W., & Oughton, S. 1999b, PhRvL, 82, 3444
Miyoshi, T., & Kusano, K. 2005, JCoPh, 208, 315
Oughton, S., Matthaeus, W. H., Dmitruk, P., et al. 2001, ApJ, 551, 565
Parker, E. N. 1958, ApJ, 128, 664
Roberts, D. A., Goldstein, M. L., Klein, L. W., & Matthaeus, W. H. 1987, JGR, 92, 12023
Roberts, D. A., Goldstein, M. L., Matthaeus, W. H., & Ghosh, S. 1992, JGR, 92, 17115
Shiota, D., Kataoka, R., Miyoshi, Y., et al. 2014, SpWea, 12, 187
Shiota, D., Tsuneta, S., Ito, H., et al. 2012, in ASP Conf. Ser. 454, Hinode-3: The 3rd Hinode Science Meeting, ed. T. Sekii, T. Watanabe, & D. Sakurai (San Francisco, CA: ASP), 375
Smith, C. W., Matthaeus, W. H., Zank, G. P., et al. 2001, JGR, 106, 8253
Totten, T. L., Freeman, J. W., & Arya, S. 1995, JGR, 100, 13
Tu, C.-Y. 1987, SoPh, 109, 149
Tu, C.-Y. 1988, JGR, 93, 7
Tu, C.-Y., & Marsch, E. 1990, JPlPh, 44, 103
Tu, C.-Y., & Marsch, E. 1993, JGR, 98, 1257
Tu, C.-Y., & Marsch, E. 1997, SoPh, 171, 363
Usmanov, A. V., Goldstein, M. L., Besser, B. P., & Fritzer, J. M. 2000, JGR, 105, 12675
Usmanov, A. V., Goldstein, M. L., & Matthaeus, W. H. 2014, ApJ, 788, 43
Usmanov, A. V., Matthaeus, W. H., Breech, B. A., & Goldstein, M. L. 2011, ApJ, 727, 84
Wang, Y.-M., & Sheeley, N. R., Jr. 1990, ApJ, 355, 726
Williams, L. L., & Zank, G. P. 1994, JGR, 99, 19229
Zank, G. P., Adhikari, L., Hunana, P., et al. 2017, ApJ, 835, 147
Zank, G. P., Dosch, A., Hunana, P., et al. 2012, ApJ, 745, 35
Zank, G. P., Li, G., & Verkhoglyadova, O. 2007, SSRv, 130, 255
Zank, G. P., & Matthaeus, W. H. 1991, PhFl, 3, 69
Zank, G. P., Matthaeus, W. H., & Smith, C. W. 1996, JGR, 101, 17093
Zank, G. P., Rice, W. K. M., & Wu, C. C. 2000, JGR, 105, 25079
Zhou, Y., & Matthaeus, W. H. 1990, JGR, 95, 10291